

This is the peer reviewed version of the following article:

Multiple crustal and mantle inputs in post-collisional magmatism: Evidence from late-Variscan S`arrabus pluton (SE Sardinia, Italy) / Secchi, Francesco; Giovanardi, Tommaso; Naitza, Stefano; Casalini, Martina; Kohút, Milan; Conte Aida, Maria; Oggiano, Giacomo. - In: LITHOS. - ISSN 0024-4937. - 420-421:(2022), pp. N/A-N/A. [10.1016/j.lithos.2022.106697]

Terms of use:

The terms and conditions for the reuse of this version of the manuscript are specified in the publishing policy. For all terms of use and more information see the publisher's website.

02/05/2024 21:47

(Article begins on next page)

LITHOS

Multiple crustal and mantle inputs in post-collisional magmatism: evidence from late-Variscan Sàrrabus pluton (SE Sardinia, Italy)

--Manuscript Draft--

Manuscript Number:	LITHOS10233R2
Article Type:	Regular Article
Keywords:	Late-Variscan magmatism; Bimodal Magmatism; dilatant shear zones; crustal sources; Sr-Nd isotopes; Neodymium crustal index
Corresponding Author:	Tommaso Giovanardi Universita degli Studi di Modena e Reggio Emilia Modena, ITALY
First Author:	Francesco Secchi, Prof.
Order of Authors:	Francesco Secchi, Prof. Tommaso Giovanardi Stefano Naitza, Prof. Martina Casalini Milan Kohút, Prof. Aida Maria Conte, Dr. Giacomo Oggiano, Prof.
Abstract:	<p>The Sàrrabus pluton is formed by multiple short-lived intrusions emplaced at about 286 Ma at shallow crustal levels within the external part of the South Variscan Orogenic Belt. A chemical and Sr and Nd isotopic study on the Variscan post-collisional magmatism from the Sàrrabus pluton reveals the repeated bimodal character of the intrusions, in which heterogeneous crustal sources and mantle-derived calcalkaline magmas are involved. Products of this magmatic activity occur as intrusive units and mafic/felsic dykes intruded in post-collisional regime along extensional faults during tectonic exhumation. Pluton growth started with an early stage of emplacement of broadly granodioritic magma with subordinate mafic magma batches (stage 1) followed by large intrusions of metaluminous to subaluminous and subordinately peraluminous granites (stage 2). In stage 1, the occurrence of remnants of stratified olivine-bearing gabbroic rocks indicates the intrusion of mafic magmas which experienced low-pressure crystal/liquid fractionation. Mafic magmas may represent an external heat supply for melting of different crustal materials belonging to an inferred Precambrian crystalline basement underlying the Paleozoic rocks of the Variscan nappe pile. Strong evidence for heterogeneous crustal sources is constrained by isotope data. Peraluminous granites and felsic dikes display initial $87\text{Sr}/86\text{Sr}$ in the range of 0.7140 ± 0.7215 and a roughly constant ϵNd_{286} (-7.4 to -7.5). Conversely, a peculiar less radiogenic character, in the range of 0.7030 ± 0.7067–5.5 ± -6.2, is observed for metaluminous to subaluminous varieties. Calculated Neodymium Crustal Index (NCI) confirmed a progressive increase in crustal magmas generation during the pluton growth, from stage 1, recording minor mixing processes between mantle- and crustal-derived peraluminous melts, to stage 2, where extensive crustal melting occurred, originating metaluminous to subaluminous granites. Possible crustal sources for metaluminous/subaluminous and peraluminous granites are (Pan-African) amphibolites and metasedimentary rocks, respectively. Two-stage depleted-mantle Nd model ages cluster at 1.4 and 1.6 Ga for metaluminous/subaluminous and peraluminous granites, respectively, well comparable with other segments of the European Variscan belt. Remarkably, last magmatic pulses resulted in widespread subalkaline bimodal mafic/felsic dykes that overlapped the Sr–Nd signature recorded by major intrusions. This similar geochemical affinity between late dykes and the first intrusives may be related to decreasing temperature in the crust, which inhibited extensive mixing processes with the upwelling melts. At the same time, the presence of felsic intrusions in the shallow crust would have prevented the rise of more primitive basic magmas, which would have consolidated at depth. Finally, the high radiogenic character of</p>

	<p>Sàrrabus mafic products, compared to coeval Variscan mafic rocks of Corsica and northern Sardinia, may be indicative of previous fractionation and mixing processes, possibly related to magmatic underplating of the lower crust. The Sàrrabus pluton is formed by multiple short-lived intrusions emplaced at about 286 Ma at shallow crustal levels within the external part of the South Variscan Orogenic Belt. A chemical and Sr and Nd isotopic study on the Variscan post-collisional magmatism from the Sàrrabus pluton reveals the repeated bimodal character of the intrusions, in which heterogeneous crustal sources and mantle-derived calcalkaline magmas are involved. Products of this magmatic activity occur as intrusive units and mafic/felsic dykes intruded in post-collisional regime along extensional faults during tectonic exhumation. Pluton growth started with an early stage of emplacement of broadly granodioritic magma with subordinate mafic magma batches (stage 1) followed by large intrusions of metaluminous to subaluminous and subordinately peraluminous granites (stage 2). In stage 1, the occurrence of remnants of stratified olivine-bearing gabbroic rocks indicates the intrusion of mafic magmas which experienced low-pressure crystal/liquid fractionation. Mafic magmas may represent an external heat supply for melting of different crustal materials belonging to an inferred Precambrian crystalline basement underlying the Paleozoic rocks of the Variscan nappe pile. Strong evidence for heterogeneous crustal sources is constrained by isotope data. Peraluminous granites and felsic dikes display initial $^{87}\text{Sr}/^{86}\text{Sr}$ in the range of 0.7140 ± 0.00215 and a roughly constant ϵNd_{286} (-7.4 to -7.5). Conversely, a peculiar less radiogenic character, in the range of 0.7030 ± 0.0067 to -5.5 to -6.2, is observed for metaluminous to subaluminous varieties. Calculated Neodymium Crustal Index (NCI) confirmed a progressive increase in crustal magmas generation during the pluton growth, from stage 1, recording minor mixing processes between mantle- and crustal-derived peraluminous melts, to stage 2, where extensive crustal melting occurred, originating metaluminous to subaluminous granites. Possible crustal sources for metaluminous/subaluminous and peraluminous granites are (Pan-African) amphibolites and metasedimentary rocks, respectively. Two-stage depleted-mantle Nd model ages cluster at 1.4 and 1.6 Ga for metaluminous/subaluminous and peraluminous granites, respectively, well comparable with other segments of the European Variscan belt. Remarkably, last magmatic pulses resulted in widespread subalkaline bimodal mafic/felsic dykes that overlapped the Sr–Nd signature recorded by major intrusions. This similar geochemical affinity between late dykes and the first intrusives may be related to decreasing temperature in the crust, which inhibited extensive mixing processes with the upwelling melts. At the same time, the presence of felsic intrusions in the shallow crust would have prevented the rise of more primitive basic magmas, which would have consolidated at depth. Finally, the high radiogenic character of Sàrrabus mafic products, compared to coeval Variscan mafic rocks of Corsica and northern Sardinia, may be indicative of previous fractionation and mixing processes, possibly related to magmatic underplating of the lower crust.</p>
<p>Suggested Reviewers:</p>	<p>Philippe Rossi COMMISSION FOR THE GEOLOGICAL MAP OF THE WORLD philippe.rossi20@gmail.com Expert of granitic intrusion and plutons.</p> <p>Laura Gaggero Universita degli Studi di Genova laura.gaggero@unige.it Expert of igneous and metamorphic petrology for Sardinia</p> <p>Vojtech Janousek charles university prague vojtech.janousek@geology.cz Expert petrologist and geochemist of granitic rocks and Variscan/post Variscan evolution</p>
<p>Opposed Reviewers:</p>	

Highlights

- The Sàrrabus pluton is formed by multiple short-lived intrusions at ca. 286 Ma;
- Pluton growth started with an early stage of broadly granodioritic composition;
- Large intrusions of metaluminous to subaluminous granites follow the granodiorites;
- During the pluton growth, a progressive increase in crustal magmas generation occurred;
- Last magmatics are subalkaline mafic/felsic dikes with major intrusions signature;

[Click here to view linked References](#)

1 **Multiple crustal and mantle inputs in post-collisional magmatism: evidence from late-Variscan**
2 **Sàrrabus pluton (SE Sardinia, Italy)**

3
4 **Secchi, F.^{1,2}, Giovanardi, T.^{3*}, Naitza, S.⁴, Casalini, M.⁵, Kohút, M.⁶, Conte A.M.⁷, Oggiano G.¹**

5
6 (1) Dipartimento Chimica e Farmacia, Via Piandanna 4, I-07100 Sassari (Italy). Università degli Studi di Sassari, Sassari
7 (Italy).

8 (2) CNR-Istituto di Geologia Ambientale e Geoingegneria, Sede Secondaria di Cagliari, Via Marengo 2, 09123 Cagliari,
9 Italy.

10 (3) Dipartimento Scienze Chimiche e Geologiche, Via G. Campi 103, I-41125 Modena. Università degli Studi di Modena
11 e Reggio Emilia, Modena (Italy).

12 (4) Dipartimento Scienze Chimiche e Geologiche, Cittadella Universitaria S. S. 554 bivio per Sestu, I-09042 Monserrato
13 (CA). Università degli Studi di Cagliari, Cagliari (Italy).

14 (5) Dipartimento Scienze della Terra, Via LA Pira 4, I-50121 Firenze. Università degli Studi di Firenze, Firenze (Italy)

15 (6) Earth Science Institute, Slovak Academy of Sciences, Dúbravská cesta 9, 840 05 Bratislava, Slovakia.

16 (7) CNR-IGAG, Sede di Roma, c/o DST Sapienza Università di Roma, P.^{1c} Aldo Moro 5, I-00185, Roma, Italy.

17
18 *Corresponding author. *E-mail address*: tommaso.giovanardi@unimore.it; <https://orcid.org/0000-0002-9953-6707>.

19
20 **Keywords:** (Late-Variscan magmatism, bimodal magmatism, dilatant shear zones, crustal sources, Sr-Nd isotopes,
21 Neodymium crustal index)

22
23
24 **Abstract**

25 The Sàrrabus pluton is formed by multiple short-lived intrusions emplaced at about 286 Ma at shallow
26 crustal levels within the external part of the South Variscan Orogenic Belt. A chemical and Sr and
27 Nd isotopic study on the Variscan post-collisional magmatism from the Sàrrabus pluton reveals the
28 repeated bimodal character of the intrusions, in which heterogeneous crustal sources and mantle-
29 derived calcalkaline magmas are involved. Products of this magmatic activity occur as intrusive units
30 and mafic/felsic dykes intruded in post-collisional regime along extensional faults during tectonic
31 exhumation. Pluton growth started with an early stage of emplacement of broadly granodioritic
32 magma with subordinate mafic magma batches (stage 1) followed by large intrusions of
33 metaluminous to subaluminous and subordinately peraluminous granites (stage 2). In stage 1, the
34 occurrence of remnants of stratified olivine-bearing gabbroic rocks indicates the intrusion of mafic
35 magmas which experienced low-pressure crystal/liquid fractionation. Mafic magmas may represent
36 an external heat supply for melting of different crustal materials belonging to an inferred Precambrian
37 crystalline basement underlying the Paleozoic rocks of the Variscan nappe pile. Strong evidence for
38 heterogeneous crustal sources is constrained by isotope data. Peraluminous granites and felsic dikes
39 display initial $^{87}\text{Sr}/^{86}\text{Sr}$ in the range of $0.7140 \div 0.7215$ and a roughly constant ϵNd_{286} (-7.4 to -7.5).
40 Conversely, a peculiar less radiogenic character, in the range of $0.7030 \div 0.7067 / -5.5 \div -6.2$, is
41 observed for metaluminous to subaluminous varieties. Calculated Neodymium Crustal Index (NCI)
42 confirmed a progressive increase in crustal magmas generation during the pluton growth, from stage
43 1, recording minor mixing processes between mantle- and crustal-derived peraluminous melts, to
44 stage 2, where extensive crustal melting occurred, originating metaluminous to subaluminous

45 granites. Possible crustal sources for metaluminous/subaluminous and peraluminous granites are
46 (Pan-African) amphibolites and metasedimentary rocks, respectively. Two-stage depleted-mantle Nd
47 model ages cluster at 1.4 and 1.6 Ga for metaluminous/subaluminous and peraluminous granites,
48 respectively, well comparable with other segments of the European Variscan belt. Remarkably, last
49 magmatic pulses resulted in widespread subalkaline bimodal mafic/felsic dykes that overlapped the
50 Sr–Nd signature recorded by major intrusions. This similar geochemical affinity between late dykes
51 and the first intrusives may be related to decreasing temperature in the crust, which inhibited
52 extensive mixing processes with the upwelling melts. At the same time, the presence of felsic
53 intrusions in the shallow crust would have prevented the rise of more primitive basic magmas, which
54 would have consolidated at depth. Finally, the high radiogenic character of Sàrrabus mafic products,
55 compared to coeval Variscan mafic rocks of Corsica and northern Sardinia, may be indicative of
56 previous fractionation and mixing processes, possibly related to magmatic underplating of the lower
57 crust.

58

59

60 **Introduction**

61 The Corsica-Sardinia Batholith (CSB) belongs to the southern Variscan belt of Europe and
62 represents a key area for studies on post-collisional evolution of this orogenic chain (Ferrè and Leake,
63 2001; Paquette et al., 2003; Cocherie et al., 2005; Rossi et al., 2009, 2015; Edel et al., 2014; Casini
64 et al., 2015a, b; Conte et al., 2017) (Fig. 1). The CSB was emplaced through a complex succession of
65 discontinuous short-lived tectonic and magmatic episodes from the late collisional stages to the post-
66 collisional collapse and exhumation of the orogenic roots. At present, a general agreement exists in
67 literature in considering the control of lithospheric shear zones on the emplacement of major intrusive
68 complexes of the CSB (Edel et al., 2014; Casini et al., 2012; 2015; Cuccuru et al., 2016), and the
69 involvement of metaigneous and metasedimentary crustal sources with subordinate mantle
70 contribution (Poli et al., 1989; Cocherie et al., 1994; Tommasini et al., 1995; Macera et al., 2011;
71 Rossi et al., 2015; Conte et al., 2017). Also, the heat source necessary to generate the large volumes
72 of crustal-derived intrusive magma in the post-collisional regime of SCB was related to lithospheric
73 delamination and asthenospheric upwelling promoting partial melting of lower crust (Gaggero et al.,
74 2007; Rossi et al., 2015). As a result, a wide range of crustal melts and hybrid varieties, mainly of
75 broadly granodioritic composition, produced by mafic/felsic magma interactions, contributed to the
76 architecture of the entire batholith. Common effect of mafic/felsic magma interaction was
77 documented by igneous dark enclaves dispersed in granodiorites and subordinately in monzogranites
78 (Poli et al., 1989; Zorpi et al., 1991; Barbey et al., 2008; Casini et al., 2015b). Mantle-derived
79 magmas, commonly intruding in the final stages of the CSB growth, are represented by gabbroic

80 magma batches and mafic dikes. The tholeiitic and calcalkaline mafic dikes spread over the whole
81 batholith, and partly within the host metamorphic basement. Even if recent radiometric ages point to
82 a substantial contemporaneity among the main intrusive events and the subalkaline mafic dike swarms
83 (Rossi et al., 2015; Conte et al., 2017), the genetic linkage between this hypabyssal activity and the
84 plutons making the batholith was never taken into consideration.

85 The Sàrrabus pluton (south-eastern Sardinia), is formed by multiple intrusions emplaced within
86 the shallow crustal levels of a fold and thrust belt along the Gondwana foreland; it shows peculiar
87 characteristics compared to the rest of the CSB due to the different geochemical affinities of the
88 magma intrusions and their coeval ages. Previous studies performed on the Sàrrabus pluton (Brotzu
89 et al., 1981, 1993; Poli and Tommasini, 1999; Ronca et al., 1999; Conte et al., 2017; Franciosi et al.,
90 2019) focused on single aspects of the pluton without proposing a global genetic model. In a recent
91 study, Secchi et al. (2021) firstly recognized the substantial contemporaneity of a wide spectrum of
92 magma pulses concentrated in a short time span, forming a relatively small pluton (400 km²), which
93 differentiate the Sàrrabus pluton with respect to others in CSB.

94 In this work, field evidence and chemical and isotopic data (Sr and Nd bulk rock and Hf in zircons)
95 are presented and discussed with data from previous studies, to constrain the petrogenesis of the entire
96 Sàrrabus pluton. We will focus on the nature of involved crustal sources which originated the granitic
97 units of the pluton and their interactions with mantle derived melts. We will propose a genetic model
98 of growth of the Sàrrabus pluton by magma ascending through lithospheric-scale shear zones active
99 in an extensional post-collisional setting which could be applied to other shallow crustal magmatic
100 complexes rooted on lithospheric shear zones.

101

102

103 **Geological setting**

104

105 *The Variscan orogenic wedge*

106 The Variscan collisional frame of Sardinia and Corsica results in a high-grade, inner, anatectic
107 complex retaining remnants of eclogite and high-pressure mafic granulite well exposed in Corsica
108 and northern Sardinia (Cruciani et al., 2015), which overthrusts a complex pile of nappes showing
109 low- to medium- grade metamorphic imprint (Fig. 1). The nappe pile in turn overrides, with general
110 top- to- southwest transport, a non-metamorphic foreland located in southern Sardinia (Carmignani
111 et al., 1994), which is commonly interpreted as a Gondwana foreland (Edel et al., 2014; Rossi et al.,
112 2015 and reference therein). This frame is the result of the early Carboniferous collision between the
113 northern Gondwana margin, and the ribbon-like collage of terranes interposed between Gondwana
114 and Laurussia after the (present time) north-directed subduction of an oceanic domain, namely the

115 Paleo-Tethys or South-Armorican Ocean (Stampfli et al., 2003; Oggiano et al., 2010; Gaggero et al.,
116 2012). The Variscan crust was thus highly heterogeneous, consisting of several assembled terranes
117 and syn-collisional plutonic intrusions. During the post-collisional evolution of the chain, the
118 Variscan crust was widely reworked in the general context of a strike slip dextral mega shear zone
119 (Casini and Funedda, 2014; Rossi et al., 2015; Edel et al., 2016). This reworking was coeval with the
120 collapse (Ruben Diez and Preira, 2016) of the previously thickened crust and by heating related to
121 slab breakoff of the north-directed subducting oceanic lithosphere as well as to shear heating (Casini
122 et al., 2012). This post collisional frame in Sardinia, similarly to the entire Variscides, went on with
123 *HT/LP* metamorphism (Kröner and Willner, 1998; Casini and Oggiano, 2008) and was accompanied
124 by intensive magmatic activity giving rise to the CSB. The magmatic activity is coeval with
125 lithospheric-scale shear zones and anatexis in the 320÷305 Ma wide interval, as well as to extension
126 and to the clockwise rotation of Corsica-Sardinia microplate (Rossi et al., 2009, 2015; Edel et al.,
127 2014).

128

129 *The Corsica-Sardinia Batholith*

130 The CSB resulted from the succession of discrete, short-lived plutonic and volcanic events of
131 broadly calcalkaline affinity, which may be grouped into three main magmatic peaks based on
132 geographic, geochronological and magmatic criteria as follows:

133 (1) late-collisional magmatic peak, only documented in western and northwestern Corsica within a
134 short time span of 344 ÷ 335 Ma (Cocherie et al., 2005);

135 (2) older post-collisional magmatic peak (hereafter OMP, *sensu* Conte et al., 2017), poorly
136 represented in southern Sardinia lasting from 322 ± 8 Ma (northern Sardinia; Casini et al., 2015a) to
137 299 ± 3 Ma (central Sardinia; Meloni et al., 2017);

138 (3) younger post-collisional magmatic peak (hereafter YMP, *sensu* Conte et al., 2017) widespread in
139 Sardinia and Corsica and referred to the short time span of 291÷286 Ma (Cocherie et al., 2005; Casini
140 et al., 2015a).

141 The igneous activity belonging to the syn-collisional peak resulted in a rock-association made up
142 of quartz monzonites to syenogranites with enclaves of ultrapotassic mafic rocks (the so-called Mg-
143 K rock-suite; Cocherie et al., 1994 and reference therein), emplaced from deep crustal levels up to
144 shallow conditions.

145 The architecture of CSB is instead closely related to the post-collisional stages of the Variscan
146 orogen. With the exception of the earlier andalusite-bearing foliated granodiorites and leucogranites
147 occurring in northernmost of Sardinia (i.e., Barrabisa and Santa Maria Island: 321 ± 8 ÷ 313 ± 6 Ma;
148 Oggiano et al., 2007; Casini et al., 2012), the OMP is characterized by repeated sequences of
149 monzogranitic and granodioritic pulses with subordinate mafic rocks, which represent the dominant

150 intrusive activity in the internal nappe zone of northern-central Sardinia. Overall, magma pulses
151 emplaced almost constantly at shallow crustal levels (about 2–4 kbar; Casini et al., 2012; Conte et al.,
152 2017; Bosi et al., 2019). Shallow conditions are constrained by the common development of narrow
153 contact aureoles with andalusite-cordierite hornfelses around the plutons, as well as by geobarometric
154 results (Conte et al., 2017; Bosi et al., 2019 and reference therein); in addition, andalusite and
155 cordierite may occur as fundamental phases in peraluminous varieties (e.g., Barrabisa and
156 Gennargentu, Fig. 1; Casini et al., 2012; Gaeta et al., 2013).

157 In the external nappe zone and in the Gondwanan foreland of southern Sardinia, the OMP is only
158 represented by small plutons with inverse zonation belonging to an ilmenite rock-*series* and ranging
159 from granodiorites to peraluminous cordierite-bearing granites (e.g., Arbus and Grighini) with local
160 small amounts of olivine-bearing monzo-gabbronorites (Arbus, Capo Pecora and Burcèi) (Secchi et
161 al., 1991; Brotzu et al., 1993; Musumeci et al., 2014) (Fig. 1).

162 The intrusive bodies belonging to YMP are dominated by voluminous (mainly NE-trending)
163 peraluminous to subaluminous felsic and minor mafic intrusions emplaced at the shallowest crustal
164 levels (about 1 kbar; Gaggero et al., 2007; Conte et al., 2017 and reference therein). Granodioritic
165 sequences associated to mafic bodies cover a restricted time span of $286 \pm 1 \div 279 \pm 1$ Ma (Paquette
166 et al., 2003; Casini et al., 2015a). The age of these late intrusions overlaps that of peralkaline granites
167 which are only exposed in northern Corsica (Cocherie et al., 2005). In southern Sardinia,
168 metaluminous to sub-aluminous granites are dominant over peraluminous granites. They mainly
169 belong to ilmenite rock-*series* and show a F-rich ferroan character as well as a peculiar metallogenic
170 signature as testified by Sn-W-Mo and F ores (Naitza et al., 2017).

171 Exposed rock-types are dominantly felsic (over 90% granodiorites and granites), with only minor
172 amounts of gabbroic rocks commonly associated with tonalites mingled with host granodiorites
173 (Zorpi et al., 1991). The production of magmas in the CSB is largely interpreted as related to
174 contemporaneous partial melting of crustal materials and interactions of felsic melts with mafic
175 magmas at several levels in the crust (Secchi et al., 1991; Zorpi et al., 1991; Tommasini and Poli
176 1992; Cocherie et al., 1994; Tommasini et al., 1995; Di Vincenzo et al. 1996; Poli and Tommasini,
177 1999; Renna et al., 2006; Barbey et al., 2008). According to Rossi et al. (2015), the voluminous felsic
178 activity marking the end of YMP in the entire CSB reflects a phase of intense crustal heating triggered
179 by lithospheric delamination and intrusion of mafic magmas in the lower crust. Heating contribution
180 in this phase has also been related to intense shearing (Casini et al., 2012; 2015b) and radiogenic
181 heating (Puccini et al., 2013).

182 The 291÷286 Ma emplacement age interval identified for YMP overlaps with U/Pb data
183 determined for *HT-LP* granulites from the Variscan deep crust exhumed along the “European” margin

184 of the thinned Tethys margin from Corsica and Calabria, which are in the range of 285–280 Ma (Rossi
185 et al., 2015).

186 Furthermore, the early Permian intrusive magmatism is coeval with calcalkaline felsic/intermediate
187 volcanism associated to the onset of continental basins in an extensional/transensional regime
188 (Cortesogno et al., 1998; Gaggero et al., 2017).

189 Based on SHRIMP analyses on zircons, the late calcalkaline mafic dykes from Corsica provided age
190 values of 279 ± 1 Ma (Cocherie et al., 2005).

191

192 *The Sàrrabus pluton*

193 The Sàrrabus pluton -exposed for over 400 km²- is formed by multiple, short-lived pulses
194 emplaced at shallow crustal levels within an anchi-metamorphosed Cambro-Ordovician volcano-
195 sedimentary sequence in the frontal part of the orogenic wedge of the SE Sardinia (Fig. 1). Its original
196 extension and shape are unknown, as the contact with the host rocks is limited to its northern boundary
197 (Fig. 2) even if small roof pendants of metamorphic basement are locally exposed along the southern
198 Sardinian coastline. The pluton may be framed in a dilatant extensional/transensional shear zone
199 bordering the Sardinia-Corsica tectonic microplate to the E (Secchi et al., 2021). It consists of
200 different generations of granodiorites, associated to gabbroic rocks and tonalites, and of
201 metaluminous, subaluminous and subordinately peraluminous granites, all referable to the YMP. The
202 pluton shows abundant mafic and felsic dikes crosscutting the main intrusions, thus representing the
203 later igneous activities.

204 The available geochronological data support a restricted time interval of emplacement for the
205 whole pluton, with ages clustered around 286 Ma (Secchi et al., 2021). In detail, U/Pb data on single
206 zircons yielded overlapping ages at 287 ± 1 Ma for the S. Vito leucogranite satellite intrusion (Dack,
207 2009) and at 286 ± 9 Ma for the Cala Regina granodiorites (Secchi et al., 2021). These ages are in
208 good agreement with Ar-Ar and Rb/Sr data available for S. Vito leucogranite and Cala Regina
209 granodiorites yielding 285 ± 1 and 292 ± 17 Ma, respectively (Dini et al., 2005; Secchi et al., 2021).

210 The geology of the pluton has been recently outlined by Secchi et al. (2021; Fig.2). The intrusive
211 sequence may be schematized as follows. The older part of Sàrrabus pluton (hereafter the *stage 1*) is
212 an intrusive sequence of EW/ENE trending pulses of granodiorites and coeval mafic batches, well
213 exposed along the southern Sardinian coastline (Fig. 2). The granodioritic pulses have been defined
214 by Secchi et al. (2021) as Cala Regina, Monte Cresia and Monte Nai units; in this study they are
215 hereafter reported together as the Cala Regina Group. In the field, size and abundance of
216 microgranular dark enclaves and frequency of mafic bodies in granodiorite increase from N to S. In
217 their southernmost outcrops, where they are intruded by the NE trending, peraluminous granite of
218 Monte Maria-Unit, granodiorites contain in addition hololeucocratic felsic enclaves (Fig. 3a).

219 The Cala Regina Group granodiorites locally grade into foliated quartz-diorite and tonalite with
220 highly stretched hybrid enclaves (Fig. 3b), dismembered syn-plutonic dikes and decametric bodies of
221 elongated two pyroxene-bearing hornblende-gabbroic rocks with local remnants of olivine-bearing
222 layers (i.e., cumulitic rocks of Solànas Complex; SO in Fig. 2). The magmatic foliation trends roughly
223 E-W and is sub-vertical or steeply dipping to the south. It is defined by the preferred orientation of
224 dark mica, feldspar and stretched microgranular mafic enclaves. The magmatic lineation, where
225 observed, plunges down dip and is defined mostly by alignment of dark mica, feldspars as well as the
226 long axis of mafic enclaves (Fig. 3b). Close to the coast, along a 2 km wide belt roughly trending E-
227 W, extremely stretched enclaves occur in large proportion along banded mafic-felsic domains (Fig.
228 3c), these features have been related to mingling processes (Poli and Tommasini 1989) enhanced by
229 a normal, syn-plutonic shear zone, namely the South Sarrabus Shear zone (SSSZ; Secchi et al 2021;
230 Fig. 2). The coeval intrusion of mafic and felsic magmas favored localized magma mixing, which
231 resulted in the local production of heterogeneous magmas of broadly tonalitic composition. This
232 magma emplaced by lateral expansion in a NS direction that is common to the other pulses (Secchi
233 et al., 2021).

234 The younger part of Sàrrabus pluton is dominated by a group of at least three different pulses of
235 F-rich ferroan granites (hereafter as *stage 2*), which intrude the granodiorites and range from biotite
236 granites (Brunco Nicola Bove Unit and San Priamo Unit) to hastingsite granites (Monte Sette Fratelli
237 Unit). The first two granitic intrusions were emplaced along an E-W trend while the Monte Sette
238 Fratelli Unit overlaps the others emplaced as a large sub-vertical stock. Contacts of the three are
239 parallel to the contact of stage 1 Monte Cresia unit with the surrounding Paleozoic metasediments.

240 This general frame is complicated by the occurrence of a bimodal subalkaline rock-association
241 made up of a several generations of NNW trending mafic and (metaluminous to subaluminous) felsic
242 dykes crosscutting an earlier generation of NE trending peraluminous felsic dikes dated at 293 ± 3
243 Ma (Ronca et al., 1999; Fig. 3e; f). Remarkably, mafic dikes consist of spessartites to hornblende-
244 bearing granular rocks and is prevalently outcropping in Cala Regina Group granodiorites exposed in
245 southern portion of the pluton. The end of Sàrrabus igneous activity is represented by a generation of
246 olivine plagioclase-phyric mafic dikes with tholeiitic signature (Ronca et al., 1999) that crosscuts
247 granite intrusions with a dominant NS trend.

248

249

250 **Analytical methods**

251 Whole-rock major and trace element concentrations of twelve samples representing the different
252 Sàrrabus lithologies were determined at Activation Laboratories, Ancaster, Ontario, Canada.
253 Powdered samples were previously fused using lithium metaborate or tetraborate, and then rapidly

254 digested in weak nitric acid solutions. Resulting solutions were analyzed by inductively coupled
255 plasma–optical emission spectroscopy (ICP–OES) and ICP–mass spectrometry (ICP–MS)
256 techniques. The uncertainties in major element concentrations are generally between 1% and 3%,
257 except for MnO (5%–10%) and P₂O₅ (>10%); most trace elements concentrations have uncertainties
258 of <5%. Major element concentrations usually have detection limits of 0.01 wt%. Loss on ignition
259 (L.O.I.) and FeO contents were measured using standards gravimetric techniques and titration with
260 10N KMnO₄ techniques, respectively. Data are reported in Supplementary Material Table 1.

261 Additional samples were analysed for major and trace elements by *XRF* spectrometry using
262 powder pellets, at the University of Cagliari laboratories, Italy. *X*-ray analyses were performed on an
263 automatic Philips spectrometer (PW1400). Data were corrected for drift and background effects.
264 Major elements were reduced for matrix effects according to Franzini et al. (1972). Trace elements
265 were reduced for matrix effects using the method of fundamental parameters according to Criss and
266 Birks (1968). Thirty reference rock standards were used for calibration. Analytical accuracy is within
267 ±1% for SiO₂, TiO₂, Al₂O₃, Fe₂O₃, CaO, K₂O and MnO, and ± 4% for MgO, Na₂O and P₂O₅. The
268 accuracy of trace element analyses is ± 2 to 3% at 1000 ppm, ± 5 to 10% at 100 ppm, and ± 10 to
269 20% at 10 ppm level. Rh and W *X*-ray tubes were used, and detection limits were around 3 ppm for
270 most trace elements. Data are reported in Supplementary Material Table 2.

271 Eleven selected samples, representing all the Sàrrabus lithologies were analyzed for Sr and Nd
272 isotopic compositions at the laboratories of Dipartimento Scienze della Terra (Università degli Studi
273 di Firenze, Italy). Sr and Nd measurements were obtained by a ThermoFisher Triton Plus multi-
274 collector mass-spectrometer, running in a static mode, following separation of Sr and Nd using
275 conventional ion-exchange procedures as reported in Avanzinelli et al. (2005). Measured ⁸⁷Sr/⁸⁶Sr
276 ratios were normalized to ⁸⁸Sr/⁸⁶Sr = 8.375209, ¹⁴³Nd/¹⁴⁴Nd ratios to ¹⁴⁶Nd/¹⁴⁴Nd = 0.7219. During
277 collection of isotopic data, replicate analyses of the Sr NIST SRM 987 (SrCO₃) isotopic standards
278 gave an average ⁸⁷Sr/⁸⁶Sr value of 0.710251 ± 20 (2σ_m, N = 100) well in agreement with the reference
279 value of Thirwall, (1991). The in-house Nd isotopic standard NdFi (Nd oxide) was used to test
280 reproducibility. Data are reported in Supplementary Material Table 3.

281 Lu–Hf analyses were performed on the same zircon crystals previously U–Pb dated by Secchi et
282 al. (2021) on SSP2 sample from Cala Regina granodiorite (Capo Carbonara, Fig. 2). Analyses were
283 done in the same dated domains and were carried out using a double focusing MC–ICP–MS with a
284 forward Nier–Johnson geometry (Thermo Fisher Scientific, Neptune™), coupled to a 213 nm
285 Nd:YAG laser ablation system (New Wave Research™) at the laboratory of Centro
286 Interdipartimentale Grandi Strumenti of the Università di Modena e Reggio Emilia. Isotopic ratios
287 were acquired in static mode with a block of 250 cycles (including laser warm-up, ~50–80 cycles of
288 analysis and washout), an integration time of 0.5 s, a laser spot of 55 μm and a fluence of ~10 J/cm².

289 A low laser frequency (~10 Hz) was used to achieve better signal stability with a He flux of ~0.5
290 L/min. Details of the method are reported in Giovanardi et al. (2018). Data reduction was performed
291 using the Hf-INATOR software (Giovanardi and Lugli, 2017). During the analytical session,
292 reference material zircon TEMORA-2 was used to check accuracy and precision. TEMORA-2
293 provides $^{176}\text{Hf}/^{177}\text{Hf}$ ratios of 0.282686 ± 0.000075 (2σ , $n=6$), identical within error to the reference
294 value of 0.282686 (Woodhead and Hergt, 2005). Data are reported in Supplementary Material Table
295 4.

296

297

298 **Results**

299 Representative samples from the intrusive units of Sàrrabus pluton have been analyzed for major,
300 trace elements and Sr and Nd systematics to integrate whole-rock data available in the literature for
301 gabbroic rocks and granodiorites (Poli and Tommasini, 1999; Franciosi et al., 2019), granitic units
302 (Conte et al., 2017), as well as for mafic and acidic dikes (Ronca et al., 1999).

303 Overall, this expanded dataset supports a new and broader petrological and evolutionary picture
304 of the pluton.

305 According to Miller (1985), in this paper granites with $\text{ASI} > 1$ ($\text{ASI} = (\text{mol. Al}/(\text{Ca}+\text{Na}+\text{K}-$
306 $1.67*\text{P})) < 1.0$) coupled with the occurrence of a more aluminous mineral phase than dark mica will be
307 classified as peraluminous.

308

309 *Essential petrographic features*

310 The main petrographic and mineralogical features of Sàrrabus igneous units are outlined in Conte
311 et al. (2017; 2018a; b and reference therein) and summarized in Fig. 4 and Tab. 1. Rocks were
312 classified according to IUGS's recommendations, using modal compositions obtained by mass
313 balance calculations (Stormer and Nicholls, 1978). In this paragraph we will briefly describe the
314 principal features of the different lithotypes, summarizing information from D'Angelo (1998), Poli
315 and Tommasini (1999), Conte et al. (2017) and Franciosi et al. (2019).

316 Petrographic differences observed in the Cala Regina granodiorites mainly consist of an increase
317 southward in (a) size and amount of dark enclaves, which compositionally range from tonalites to
318 hornblende quartz-gabbros, (b) color index (from 14% to 20%), as well as (c) abundance of primary
319 Fe-hornblende (1%-4%; $\text{Mg}\#_{0.40-0.36}$), respectively. Typical plagioclase feldspar is a light-coloured,
320 slightly zoned andesine (An_{45-41}), even if patchy zoned plagioclases with relic of calcic cores (An_{63-}
321 39 ; Fig. 4f) are locally observed especially in biotite granodiorites. Common accessory phases are
322 well-developed euhedral allanite, associated with mafic minerals, zircon, monazite, and minor apatite
323 + ilmenite as inclusion on brownish dark mica.

324 Dismembered mafic masses in granodiorites (Solanas Complex of Cala Regina Group
325 granodiorites) are hornblende gabbroic rocks with relics of ortho- and clinopyroxene, grading to
326 hornblende quartz gabbros. These latter represent the typical composition of dark enclaves (Fig. 4a),
327 and usually show panidiomorphic and fluidal textures characterized by calcic plagioclase (An_{84-45})
328 with cotectic relationships with Fe-hornblende ($Mg\#_{0.55-0.48}$), dark mica ($Mg\#_{0.48-0.45}$) and interstitial
329 quartz (Fig. 4b). The mafic masses also include olivine-bearing gabbroic rocks and leuco-gabbros with
330 cumulate textures (Conte et al., 2018b; Secchi et al., 2021), which document a dismembered formerly
331 stratified sequence. Cumulitic rocks show commonly poikilitic textures; the dominant mineral
332 assemblage is homogeneous olivine (Fo_{74}) with peritectic relationships with orthopyroxene
333 ($Wo_{2}En_{77}Fs_{21}$) followed by calcic plagioclase (An_{89-92}) and clinopyroxene ($Wo_{47-42}En_{45-49}Fs_{8-9}$) set in
334 a dominant mass of amphibole of pargasitic composition (Fig. 4c).

335 Strong petrographic variations are observed within felsic rock-types in terms of mafic mineralogy,
336 feldspar composition as well as typical accessory phases. In detail, granites at the core of Sàrrabus
337 pluton (i.e., Bruncu Nicola Bove Unit -BNB in Fig. 2) range from biotite monzogranite to
338 leucogranite with normal oligo-albitic plagioclase (An_{30-15}). Conversely, the San Priamo granite is
339 made up of coarse-grained pinkish biotite leucogranite showing a slightly less sodic plagioclase
340 feldspar (An_{40-26}), large allanite grains and magnetite as typical accessory phases; additional
341 interstitial dark or, less frequently, white micas are often observed (Fig. 4g).

342 The Monte Maria granite is a garnet-bearing ($Alm_{65-69}Sp_{22-27}Py_5Gr_3$) two-mica variety, locally
343 containing altered cordierite (Fig. 4h), whereas the Monte Sette Fratelli Unit consist of leucogranite
344 grading to monzogranite containing oligo-albitic plagioclase (An_{20-15}), large euhedral Fe-hastingsite
345 and red-brown dark micas as early crystallized phases. Main accessory phases are large allanite +
346 magnetite + ilmenite, mostly included in amphiboles, abundant zircons included in quartz and K-
347 feldspars and anhedral fluorite grains as interstitial phases. In these rocks, dark mica of annitic
348 composition, also occurs as interstitial phase, or as discontinuous coronas on interstitial and altered
349 fayalite grains (Conte et al., 2017).

350 Main petrographic information on mafic and felsic rocks in dike swarms is outlined by Ronca et
351 al. (1999). Overall, dike swarms recorded similar features observed for compositionally-equivalent
352 intrusive rocks. Generally, the NE trending peraluminous felsic dikes, which predate the other dike
353 swarms, resemble the Monte Maria peraluminous granites: they are characterized by oligo-albitic
354 plagioclase and perthitic orthoclase with minor amounts of dark and white mica and/or spessartine-
355 rich garnet. Remarkably, rare corroded andalusite with continuous coronas of white mica are
356 occasionally observed. Apatite, zircon, monazite, magnetite and locally tourmaline are the typical
357 accessory phases.

358 Mafic dikes include rocks of dominant basaltic andesite to andesite composition, with minor
359 amounts of basalts. Overall, an orthopyroxene + clinopyroxene succession replaced by amphibole, is
360 frequently observed in the spessartitic mafic dikes (Fig. 4d); when observed, olivine occurs as
361 completely altered phenocrysts. Locally basaltic rock-types display glomero-porphyritic which may
362 be evidence of cumulitic character.

363 The final generation of basaltic dikes (tholeiitic basalt *sensu* Ronca et al., 1999) are commonly
364 characterized by labradoritic plagioclase feldspar, altered olivine and augite set in a fine-grained
365 matrix of augite, plagioclase, and minor amount of amphibole.

366

367 *Whole rock chemistry*

368 Major and trace-element chemical compositions of selected samples are reported in
369 Supplementary material Tables 1 and 2. Supplementary material Table 1 reports ICP-MS data for 9
370 specimens from main intrusive units and 3 representative samples from mafic dikes emplaced in
371 granodiorites. Supplementary Material Table 2 refers to additional unpublished *XRF* data while
372 Supplementary Material Table 5 reports average *XRF* analyses of intrusive units calculated on both
373 our analyses and literature data (Pirinu 1994, D'Angelo. 1998).

374 Gabbroic and mafic dikes rocks have medium-K character while medium- to high-K character is
375 observed for quartz-gabbroic varieties (Fig. 5a). Gabbroic rocks and analyzed mafic dikes
376 (Supplementary Material Table 1) may be defined as high alumina basalts (Fig. 5b) and show in
377 addition the prevalence of Na₂O over K₂O as a common feature: Na₂O/K₂O ratio decreases from 2.45
378 to 1.48 in olivine-bearing gabbros to quartz-gabbros, respectively, and from 2.95 to 1.90 in mafic
379 dikes. In addition, gabbroic rocks show an abrupt increase of FeO/(FeO + MgO) and Na₂O + K₂O –
380 CaO (modified alkali index) with SiO₂ from olivine-bearing gabbroic rocks to quartz gabbroic
381 varieties (Fig. 5d).

382 Conversely, granodiorites and granites are plotted at the end of a high-K rock-series (Fig. 5a) and
383 show a general increase of peraluminous character with SiO₂ evidenced by ASI in the range of 0.73
384 ÷ 0.98 (in granodiorites) with a higher value of 1.05 in garnet-bearing granite (Supplementary
385 Material Table 1). A prevalence of K with respect to Na is displayed in granodiorites and garnet-
386 bearing granite in the restricted range of 0.72 ÷ 0.74 and 0.61, respectively (Supplementary Material
387 Tables 1 and 5). In the Frost's and Frost (2001) discrimination diagrams, granodiorites display a
388 magnesian/calc-alkalic signature while granites straddle along the ferroan/alkali-calcic fields (Fig.
389 5c; d).

390 REE normalized contents of different rock-lithotypes show a similar LREE enriched pattern and
391 are poorly fractionated in MREE and HREE (Supplementary Material Table 1; Fig. 6). However,
392 some differences could be noticed. Rocks from gabbroic association show a slight decrease of the Eu

393 negative anomalies from two pyroxene-bearing gabbros ($\text{Eu}/\text{Eu}^* 0.79 \div 0.81$) to quartz gabbros
394 ($\text{Eu}/\text{Eu}^* 0.63 \div 0.74$, Supplementary Material Figure 1). Quartz gabbros and two-pyroxenes gabbros
395 display less LREE fractionation ($\text{La}_\text{N}/\text{Sm}_\text{N}$ ($1.42 \div 2.00$ in quartz gabbros and 1.6-2.2 in two pyroxene
396 bearing-gabbros) with respect to other gabbroic rocks (Fig. 6). Generally, a direct correlation is found
397 between the Eu anomaly and the $\text{La}_\text{N}/\text{Yb}_\text{N}$ ratio, while this latter is inversely correlated to the $\text{Gd}_\text{N}/\text{Yb}_\text{N}$
398 (Supplementary Material Figure 1). Cumulate rocks show Eu/Eu^* values around 1 and $\text{La}_\text{N}/\text{Sm}_\text{N}$ in
399 the range of $1.9 \div 2.9$.

400 Trace elements normalized patterns for gabbroic rocks show negative anomalies for Nb, Ta, P, Ti
401 and Sr and enrichments in more incompatible elements (i.e., Rb, Ba, Th and U; Fig. 7a).

402 Granodioritic rocks show fractionated LREE ($\text{La}_\text{N}/\text{Sm}_\text{N}$ between 2.90 and 4.33) and higher
403 $\text{La}_\text{N}/\text{Yb}_\text{N}$ (between 8.02 and 13.53) than mafic rocks, with slightly more pronounced Eu anomalies
404 (Eu/Eu^* average of 0.67) (Fig. 6b). In addition, trace elements show depletion for Nb, Ta, Sr and P,
405 and high fractionation for the more incompatible elements (Rb, Ba, Th and U), along with peaks in
406 Sr (Fig. 7b).

407 Granitic rocks display fractionated LREE, relatively flat HREE patterns with $\text{Gd}_\text{N}/\text{Yb}_\text{N}$ values range
408 from 0.95 to 1.45 (Supplementary Material Table 1). Eu/Eu^* decrease from 0.33 in Monte Sette
409 Fratelli and San Priamo metaluminous/subaluminous granites to 0.18 in Monte Maria Unit
410 peraluminous granite (Fig. 6b). In detail, granites from Monte Sette Fratelli Unit are more enriched
411 in REE and show a slight fractionation in HREE. Conversely, granites from San Priamo Unit are less
412 enriched in REE and show a convex pattern for M-HREE (Fig. 6d). The picture is complicated by the
413 peraluminous granite (Monte Maria), which shows fractionated enrichment for LREE from La to Nd
414 and almost flat trend from Sm to Lu (except for the Eu negative anomaly), showing LREE contents
415 lower than other granites but HREE almost comparable with those observed for Monte Sette Fratelli
416 granites (Fig. 6d). It is also the only lithology displaying Ba depletion while it also shows Nb, Sr and
417 P negative anomalies (Fig. 7b).

418 Mafic dykes (basalts to andesite-basalt in composition) show fractionated REE patterns with
419 LREE enrichments ($\text{La}_\text{N}/\text{Yb}_\text{N}$ between 5.94 and 8.35) and weak or none Eu anomaly (Eu/Eu^* between
420 1.05 and 0.83). Trace elements are depleted in Nb, Ta and P, and the more primitive dykes have a
421 positive Sr anomaly which became negative in the more evolved ones (Fig. 7a).

422 With respect to the studied samples, the late felsic dykes show the most heterogeneous REE contents
423 (Fig. 6d). Different REE compositions, which basically overlap both metaluminous and peraluminous
424 granites, point out to several different sources of the parent melts.

425

426 *Isotope data*

427 Sr and Nd isotopic ratios (Supplementary Material Table 3) have been calculated back to 286 Ma
428 the likely age for intrusive rocks and mafic to felsic dykes (Secchi et al., 2021) assuming a
429 substantially rapid emplacement of magmatic pulses based on the field evidence on the intrusion
430 sequence, as well as on geochronological data.

431 When schematizing the Sàrrabus pluton as composed by an older *stage 1* and by a younger *stage*
432 *2*, the isotope composition may be discussed as follows.

433 Granodiorites and associated gabbroic rocks show no correlation between $1/\text{Nd}$ and $^{143}\text{Nd}/^{144}\text{Nd}$
434 initial values (Supplementary Material Figure 2), as well as between SiO_2 and $^{87}\text{Sr}/^{86}\text{Sr}_t$ and $\epsilon\text{Nd}_{(t)}$
435 (not shown). In addition, in the $^{87}\text{Sr}/^{86}\text{Sr}_t$ vs. $\epsilon\text{Nd}_{(t)}$ diagram (Fig. 8) granodiorites plot in a restricted
436 field, ranging from 0.7088 to 0.7097 and from -5.5 to -6.3 , respectively. Remarkably, gabbroic rocks
437 commonly show more radiogenic values for Nd and range in composition from 0.7081/ -5.9 to
438 0.7099/ -6.8 ; overall, a similar behavior is observed in the $1000/\text{Sr}$ vs. $^{87}\text{Sr}/^{86}\text{Sr}_t$ diagram
439 (Supplementary Material Figure 2). A partial overlap in isotopic data between these groups of rocks
440 is represented by tonalites, confirming field observations of mingling relationships with gabbroic
441 rocks.

442 In the Rb-Sr and Nd-Sm isochron plot (Supplementary Material Figure 3), only the granodioritic
443 rocks and microgranular quartz-gabbros cluster on a 286 Ma reference line (according to published
444 Pb/Pb chronological data: Secchi et al., 2021), whereas gabbroic rocks show scattered values.

445 Peraluminous granites belonging to Monte Maria and peraluminous rhyolitic dikes show constant
446 $\epsilon\text{Nd}_{(t)}$ (-7.5) and extremely high $^{87}\text{Sr}/^{86}\text{Sr}_t$ in the range of $0.7154\div 0.724$, respectively, which approach
447 to a supracrustal endmember.

448 Metaluminous to sub-aluminous granite rock-types belonging to *stage 2* (i.e., Monte Sette Fratelli
449 and San Priamo), which occupy the northern side of the pluton, form an independent group showing
450 a flat trend in the Sr–Nd diagram (barred symbols in Fig. 8; Conte et al., 2017). They exhibit a wide
451 Sr isotopic composition, from 0.703 to 0.7095 and, conversely, a quite homogeneous $\epsilon\text{Nd}_{(t)}$ value of
452 about -7.5 that does not differ from the field of metaluminous felsic dikes reported in Ronca et al.
453 (1999).

454 In general, in the $^{87}\text{Sr}/^{86}\text{Sr}_t$ vs. $\epsilon\text{Nd}_{(t)}$ diagram (Fig. 8), mafic dikes overlap the trend described by
455 the entire *stage 1* ranging from 0.7068/ -2.9 to 0.7097/ -6.2 . It is to be noticed that lesser and roughly
456 constant radiogenic compositions ($0.7053\div -1.35$) are recorded for late mafic (tholeiitic) dikes hosted
457 in leucogranites.

458 Further petrogenetic information may be provided by the Nd crustal residence ages for granites
459 and basaltic dikes, on account of a crustal origin proposed in literature (Ronca et al., 1999; Conte et
460 al., 2017) and of mafic/felsic magma interactions described in the previous geological section,

461 respectively. Given the observed linear correlation between Sm/Nd and two-stage Nd crustal
462 residence age, a two-stage model is here preferred. Overall, calculated model ages are in the 1.4 – 1.6
463 Ga range reported for European Variscan chain (Janoušek et al., 1995; Downes et al., 1997; Villaseca
464 et al., 1998). In detail, two-stage Nd crustal residence ages calculated for basaltic dikes are in the
465 range of 1.25 – 1.61 Ga and decrease to 1.11 in olivin-phyric tholeiitic basalts.
466 Metaluminous/subaluminous granites and dikes are in the range of 1.44 ÷ 1.50 Ga; higher values
467 clustered to 1.59 Ga have been obtained for peraluminous granites and dikes.

468 On the granodiorite sample dated by U-Pb zircon ages by Secchi et al. (2021), Lu-Hf analyses on
469 dated zircons were performed (Supplementary Material Table 4 and Figure 4). $^{176}\text{Hf}/^{177}\text{Hf}$ ratios for
470 Cala Regina granodiorite (sample SPP2) are between 0.282441 and 0.282621. $\varepsilon\text{Hf}(t)$ recalculated back
471 at 286 Ma (Secchi et al. 2021) provided negative values, between -5.6 and -1.0, but a single positive
472 value was also found at 0.5.

473

474

475 **Discussion**

476

477 *Geological constraints for Sàrrabus magmatism*

478 The emplacement of Sàrrabus pluton occurred in a crustal segment likely made up of an ancient
479 (Proterozoic) basement belonging to northern Gondwana margin overthrust by Paleozoic nappes
480 dominated by Cambro-Ordovician anchimetamorphic sedimentary rocks (Carmignani et al., 1994;
481 Edel et al., 2014).

482 Field (Secchi et al., 2021) and geochronological data discussed in the previous geological section
483 provide evidence of rapid emplacement at shallow crustal levels (1-2 kb: Conte et al., 2017; Secchi
484 et al., 2021) of a wide variety of compositionally different magma pulses: (a) mafic/granodiorite
485 mingling relationships, the lack of contact metamorphic aureole and syn-magmatic deformation ; (b)
486 granitic pulses that unconformably crosscut granodiorite flat intrusions with steep contacts; (c)
487 undistinguishable ages, clustered at 286 Ma, based on several isotopic systematics on *stage 1* and
488 *stage 2* units (Nicoletti et al., 1982; Di Vincenzo et al., 2005; Dack, 2009; Secchi et al., 2021); (d)
489 occurrence of substantially coeval bimodal basaltic/rhyolitic dikes.

490 *Stage 1* melt ascending is controlled by a dilatant roughly EW trending shear zone (the SSSZ) that
491 acted as a feeder for magmas and records mingling relationships between granodiorites and gabbroic
492 magmas. Indeed, the dilatant style of the SSSZ channelized the migration of large volumes of mantle-
493 derived magmas up to upper crustal levels. Moreover, a close field association with peraluminous
494 granites is observed (i.e., Monte Maria Unit; Fig. 2). Conversely, a succession of independent granitic
495 magma pulses that share a common F-rich ferroan character marks the *stage 2* (Fig. 5d). In this stage,

496 mantle-derived magmas are only represented by few mafic dike swarms, representing a late
497 generation of olivine-plagioclase phyric basalts with tholeiitic affinity (Ronca et al., 1999; Conte et
498 al., 2017).

499

500 *Petrogenetic constraints for Sàrrabus magmatism*

501 Several lines of evidence support for the Sàrrabus pluton an early involvement of mantle-derived
502 magmas and a progressive more relevant production of crustal-derived magmas. Overall, each rock-
503 types shows distinctive petrographic and chemical characters which suggest independent evolution
504 paths.

505 Petrographic data allow to constrain the evolution of different magma pulses to upper crustal
506 levels. Evidence in favor of a general low-pressure evolution for mafic magmas hosted in Cala Regina
507 Group (<5 kbar) is the early appearance of orthopyroxene followed by calcic plagioclase and
508 clinopyroxene; in addition, olivine shows peritectic relationships with orthopyroxene (Conte et al.,
509 2018a). The increase of water content in melts, testified by amphibole + dark mica segregation,
510 characterizes the quartz gabbroic varieties; moreover, amphibole (Fe-hornblende) and dark mica of
511 similar composition become the only mafic minerals within the assemblage of granodiorites.

512 Generation of different granitic magmas is constrained by the occurrence of garnet, muscovite and
513 rare cordierite in Monte Maria Unit peraluminous rocks and, conversely, by the early appearance of
514 hastingsite in metaluminous granites (Monte Sette Fratelli Unit). An upper limit of 5 kb for magma
515 evolution (e.g., Green, 1977; Dahlquist et al., 2007 and references therein) is further confirmed for
516 Monte Maria granite by homogeneous garnet compositions (spessartine contents > 10%), coexisting
517 with cordierite.

518 Isotopic data constrain a general model for Sàrrabus magmatism. Sr–Nd systematics well
519 document the contrasting behavior between two different groups of crustal-derived (peraluminous
520 and metaluminous/subaluminous) granitic magmas and a small homogenous granodiorite field
521 unrelated to the higher variation of the trend displayed by gabbroic magmas (Fig. 8). In addition,
522 further evidence in favor of an independent origin between the mafic and granodioritic suites forming
523 the Cala Regina Group is provided by serial affinity (Fig. 5c) and REE normalized patterns (Fig. 6a).
524 In detail, the gabbroic rocks are generally LREE-enriched with respect to granodiorites; conversely,
525 cumulitic varieties suggest that the segregation process for gabbroic parent melts produced a decrease
526 in the LREE content. Granodiorites are more fractionated in LREE with respect to gabbroic rocks,
527 but also show a more pronounced negative Eu anomaly, thus indicating that plagioclase fractionation
528 in granodiorites has differently affected the REE compositions. The dual signature of gabbroic rocks
529 pointing to none, or small segregation of plagioclase indicates different *P-T* conditions for the parental
530 melts during fractionation, thus suggesting a vertically zoned magmatic reservoir.

531 In a general extensional setting, the ascent of gabbroic magmas at middle/upper crustal levels may
532 provide the necessary heat input to cause dehydration melting of biotite and muscovite in
533 metasedimentary rocks and promotes the generation of peraluminous granitic melts belonging to the
534 *stage 1*. In this scheme, evidence in favour of a source located in the middle crust is the general low-
535 pressure (<5 kbar) evolution indicated for gabbroic magmas by textural relationships. In addition,
536 generally flat REE patterns lead to exclude a garnet-bearing source.

537 As expected by geological relationships and petrographic characters, mafic and felsic dike swarms
538 overlap the trends observed for rocks belonging to *stage 1* and *stage 2*, respectively.

539 A genetic model involving contamination and crystal/liquid fractionation process has been already
540 proposed to explain the magmatic evolution observed for gabbroic magmas of Scala Carbonara body
541 (SC in Fig. 2) contaminated by granodioritic magma (Poli and Tommasini, 1999). The different
542 behavior of gabbroic and granodioritic magmas point to different compositions and evolutions of the
543 parent melts. Overall, an enriched mantle source is inferred from Ta/Yb–Th/Yb plot for gabbroic
544 magmas and for selected mafic dikes from Sàrrabus pluton, in agreement with data reported by
545 Gaggero et al. (2007) for lamprophyric dikes from northern Sardinia (Supplementary Material Figure
546 5). In addition, mafic rocks of the Sàrrabus pluton shows several degrees of crustal assimilation as
547 revealed by Rb, Ba, Th and U concentrations which are relatively high and negative ϵ_{Nd} also in
548 cumulate gabbroic rocks (Fig. 7). This implies consequences with regard to isotope ratios: Nd model
549 ages for these rocks are actually meaningless, being calculated on mixed isotopic composition derived
550 by several sources. Moreover, different isotopic trends displayed by gabbroic rocks and granodiorites
551 suggest that the mantle-derived melts interacted with different crustal components and could be re-
552 equilibrated at different crustal levels.

553 According to Conte et al. (2017), metaluminous to sub-aluminous granitic magmas require
554 processes of partial melting involving lower crustal level of mostly intermediate/mafic composition,
555 as confirmed by whole-rock initial Pb isotopic compositions of metaluminous to subaluminous
556 granites (i. e., San Priamo and Monte Sette Fratelli units which plot in the lower crust field in the
557 $^{206}Pb/^{204}Pb$ – $^{208}Pb/^{204}Pb$ plot in Conte et al., 2017).

558

559 *Evaluating the involvement of crustal materials*

560 An essential assumption of our models of magma genesis and the relation to Nd isotopes is the
561 involvement of pre-existing continental crustal material (with low ϵ_{Nd} and relatively high Nd
562 concentration) and/or contribution from sub-continental lithospheric mantle (SCLM) (with high ϵ_{Nd}
563 and moderate Nd concentration) in the generation of mafic and granitic magmas. The $^{147}Sm/^{144}Nd$
564 ratio in a reservoir is expressed as the enrichment factor relative to CHUR as $f_{Sm/Nd} =$

565 $(^{147}\text{Sm}/^{144}\text{Nd}_{\text{sample}})/(^{147}\text{Sm}/^{144}\text{Nd}_{\text{CHUR}}) - 1$ after De Paolo and Wasserburg (1976). According to De
566 Paolo et al. (1992) the fractional isotopic shift from mantle (MC) to crustal (CC) ϵNd values can be
567 described by the Neodymium Crustal Index (NCI): $\text{NCI} = [\epsilon\text{Nd}(\text{rock}) - \epsilon\text{Nd}(\text{MC})]/[\epsilon\text{Nd}(\text{CC}) -$
568 $\epsilon\text{Nd}(\text{MC})]$. NCI thus describes the fraction of crustal Nd in a rock. NCI is 0 when the rock has no
569 crustal Nd (the ϵNd value is equal to the mantle MC source value) and 1 when all Nd in a rock has a
570 crustal origin (the ϵNd value is equal to the crustal CC value). Surveying local data, we have
571 considered MC = +8 and CC = -15 for NCI calculation, representing MC – an average composition
572 of the YMP mafic rocks from Sardinia (Gaggero et al., 2007), and CC – composition of the most
573 crustal metasedimentary schist from the Sardinia basement (Di Vincenzo et al., 1996). Nd isotopic
574 compositions of mafic/felsic rocks from Sàrrabus pluton and available data from entire Sardinia range
575 from near model mantle values to near model crustal values (Fig. 9a). Moreover, collected data show
576 slightly negative correlation in the $f_{\text{Sm}/\text{Nd}}$ vs. NCI plot, and partial coincidence of mafic rocks with
577 granitic rocks. The abnormally high NCI = 0.62–0.75 for the mafic rocks was likely caused by fluid-
578 metasomatism of pre-existing SCLM or related to contamination with (amphibolitic) lower crust.
579 This enrichment is obvious from $f_{\text{Sm}/\text{Nd}}$ vs. $\epsilon\text{Nd}_{(286)}$ plot (Shirey and Hanson, 1986; Fig. 9b) where
580 both mafic and felsic rocks from Sàrrabus pluton lie in the quadrant characterized by crustal
581 enrichment (i. e. negative $f_{\text{Sm}/\text{Nd}}$ and $\epsilon\text{Nd}_{(i)}$ values; Fig. 9b).

582 Such mafic/felsic intrusions, that have initial Nd isotope ratios below to the chondritic value (ϵNd
583 < 0), indicate possible SCLM sources that are chemically enriched/metasomatized, and thus different
584 from the MORB or volcanic-arc basalt sources. Although the Sr–Nd isotopic characteristics of
585 particularly mafic components are quite atypical, nevertheless it is possible to model the mixing
586 between the mafic component (sample SSP6b from a mafic dike) and the crustal ones (sample SSP59,
587 from peraluminous granite; Fig. 10). Obviously, from the presented model, the crustal source is
588 dominant (80–85%) in the genesis of granodioritic magmas, as also supported by negative $\epsilon\text{Hf}(t)$
589 values, while the concomitant mafic components with unusually high negative $\epsilon\text{Nd}_{(286)}$ over -4 (Figs
590 8 and 10) show considerable crustal enrichment or fluid-metasomatism.

591 This large involvement of crustal materials is coherent with negative ϵHf values of granodiorites
592 zircons and the large compositional gap emerging from Sr–Nd systematics for Corsica and northern
593 Sardinia granitoids with respect to Sàrrabus pluton (Fig. 8), that was inherited from deep sources of
594 granite magmas and related to the thermal structure of different lithospheric fragments assembled
595 during the Variscan collision in the Sardinia-Corsica massif. The more radiogenic signature and the
596 value of $\delta^{18}\text{O}_{\text{SMOW}} = +8.4 \text{ ‰}$ (Brotzu et al., 1981) observed for mafic suites and associated
597 granodiorites from Sàrrabus pluton does not conflict with an earlier contamination stage and different
598 residence times at lower crustal levels with respect to the northern Sardinia/Corsica suites.

601 When considering the genesis and emplacement of Sàrrabus magmas, which belong to a reworked
602 crust of the northern Gondwana margin thinned during the collapse and exhumation of the Variscan
603 chain (Casini and Oggiano, 2008; Rossi et al., 2015), a complex petrological model can be depicted.
604 Schematically, in a commonly accepted regime of lithospheric mantle delamination (Edel et al., 2014;
605 Rossi et al., 2015), extensional shear zones, as the SSSZ, favoured the repeated ascents of mantle-
606 derived magmas which experienced crystal/liquid fractionation (Poli and Tommasini, 1999; Conte et
607 al., 2018; Franciosi et al., 2019) and likely served as a heat source for melting of metasedimentary
608 crustal levels, producing peraluminous granite magmas in *stage 1*.

609 Tommasini et al. (1995) pointed out that the main geochemical characters of the Sardinian high-
610 K and I-type calcalkaline granitoids suggest a dominant derivation from partial melting of
611 metigneous and igneous-derived materials belonging to a volcanic arc linked to an Ordovician
612 subduction. Remarkably, this group of granites and rhyolitic dikes overlaps the field of felsic
613 granulites belonging to the Central Spanish Variscan System (Villaseca et al., 1998); an overlap with
614 lower crustal sources was also inferred by Pb isotopic data obtained for SPU leucogranites. According
615 to Conte et al. (2017), granitic rocks like MSFU, which plot in the III quadrant of $^{87}\text{Sr}/^{86}\text{Sr}_t$ vs. $\epsilon\text{Nd}(t)$
616 diagram, have isotopic values which are rather uncommon at the scale of entire European Variscides.

617 Accordingly, the two-stage T_{DM} crustal residence ages calculated for Sàrrabus granites overlap
618 those calculated for Cambro-Ordovician orthogneisses from northern Sardinia and central Iberia (Di
619 Vincenzo and Ghezzo, 1996; Villaseca et al., 1998). On the other hand, the geochemical/metallogenic
620 and lead isotopic signatures of the F-rich, ferroan granites indicates the derivation from meta-igneous
621 sources in the lower crust (Conte et al., 2017). This provenience from a deep source for the
622 metaluminous/subaluminous products of the Sàrrabus pluton *stage 2* may also assume the
623 significance of a possible derivation from an inferred and more ancient (Proterozoic) volcanic arc,
624 rooted in a crystalline basement under the cover of Paleozoic nappes.

625

626

627 **Conclusions**

628 The Sàrrabus pluton documents a sequence of magmatic events which record a repeated bimodal
629 character in which different mantle-derived and crustal-related magmas, whose ascent was controlled
630 by dilatant extensional faults, are recognized. Several lines of evidence suggest a complex frame of
631 mafic magmas promoting partial melting of continental crust, as well as continuous mafic/felsic
632 magma interactions decreasing in time at different crustal levels. In the general late orogenic context
633 of the frontal zone of the Variscan wedge, it is possible to hypothesize different scenarios capable of

634 explaining thermal anomalies and magma production. Radiogenic heating of previous thickened crust
635 and shear heating are mechanisms that can account for the heat supply consistent with generation of
636 large volume of crustal melts. LID delamination is a further mechanism that from syn- to post-
637 collisional settings can transfer large amount of heat from the mantle into the crust of evolving
638 orogenic belts. Delamination models may be applied to the Variscan granitic provinces even in
639 absence or scarcity of mantle magmas. Indeed, mixing processes, assimilation and mingled zones are
640 clues for mantle contributes to the building of the Variscan batholiths, including the Corsica-Sardinia
641 Batholith. The Sàrrabus pluton intruded at 286 Ma in a slightly thickened frontal portion of the
642 orogenic wedge, where low levels of radiogenic heating are expected and syn-intrusive shear heating
643 is not documented. Therefore, these two heat sources can hardly account for the melting of the crust
644 in this part of the Variscan chain. Conversely, the progressive migration of delamination away from
645 the suture zone located in Northern Sardinia, down to Central-Southern Sardinia and Sàrrabus, could
646 have heated the crust up to temperatures close to 1000 °C, which might lead to crustal melting at
647 different crustal levels. A further hypothesis may consider the high heat flux produced by a possible
648 lithosphere necking triggered by pre-existing weak zones in the mantle, determining astenospheric
649 uplift to the crust base; the far field stress able to initiate necking in an already stiffed Variscan crust
650 could be envisaged in the plate reorganization the led to the Pangaea.

651 Whatever was the actual large-scale heating mechanism, stretching conditions of Sàrrabus crust
652 favored the partial melting of different crustal levels by a heat input from mantle-derived gabbroic
653 magmas. In this context, a regime of decreasing temperature of the crust may account for the marked
654 bimodality of diking activity, which inhibits the production of voluminous granodioritic magmas by
655 mixing processes.

656

657 **Acknowledgements**

658 This work was supported by Fondo di Ateneo per la Ricerca -FAR2019- (Università di Sassari.
659 Sassari, Italy), RAS L.R. 7/2007 research program ‘Il blocco Sardo-Corso: area chiave per la
660 ricostruzione della geodinamica Varisica’ CUP J81G17000110002 and by RAS/FdS research
661 program “Sustainable land management: the tools of geology for the environment” - CUP
662 F75F21001270007). Special thanks to FO.RE.S.T.A.S. for the access to the natural reserve of Monte
663 Sette Fratelli, to Mattia Alessio Meloni for some outcrop pictures and to Daniele De Lisa for part of
664 the graphic work.

665
666
667
668
669
670
671
672
673
674
675
676
677
678
679
680
681
682
683
684
685
686
687
688
689
690
691
692
693
694
695
696
697
698
699
700
701
702
703
704
705
706
707
708
709
710
711
712
713
714
715
716
717
718
719
720

REFERENCES

1. Avanzinelli, R., Boari, E., Conticelli, S., Francalanci, L., Guarnieri, L., Perini, G., Petrone, M.C., Tommasini, S., Ulivi, M. (2005). High precision Sr, Nd and Pb isotopic analyses using the new generation Thermal Ionisation Mass Spectrometer ThermoFinnigan Triton-Ti®. *Periodico di Mineralogia*, 74(3), 147-166.
2. Barbey, P., Gasquet, D., Pin, C., Bourgeix, A. L. (2008). Igneous banding, schlieren and mafic enclaves in calcalkaline granites: The Budduso pluton (Sardinia). *Lithos*, 104, 147-163.
3. Baxter, S., Feely, M. (2002). Magma mixing and mingling textures in granitoids: Examples from the Galway Granite, Connemara, Ireland. *Mineralogy and petrology*, 76, 63-74. DOI:10.1007/s007100200032.
4. Bosi, F., Naitza, S., Secchi, F., Conte, A. M., Cuccuru, S., Andreozzi, G. B., Skogby, H., Hålenius, U. (2019). Petrogenetic controls on the origin of tourmalinite veins from Mandrolisai igneous massif (central Sardinia, Italy): Insights from tourmaline crystal chemistry. *Lithos*. 342–343, 333–344.
5. Brotzu, P., Ferrini, V., Masi, U. (1983). Stable isotope geochemistry of Hercynian granitoid rocks from the Sarrabus massif (southeastern Sardinia, Italy). *Chemical Geology*, 41, 77–90.
6. Brotzu, P., Callegari, E., Secchi, F. (1993). The search for the parental magma of the high-K calcalkaline igneous rocks series in the southernmost Sardinia batholith. *Periodico di Mineralogia*, 63, 253-280.
7. Carmignani, L., Carosi, R., Di Pisa, A., Gattiglio, M., Musumeci, G., Oggiano, G., Pertusati, P. C. (1994). The Hercynian chain in Sardinia (Italy). *Geodinamica Acta*, 7, 31-47. doi.org/10.1080/09853111.1994.11105257.
8. Casini, L., Funedda, A. (2014) – Potential of pressure solution for strain localization in the Baccu Locci Shear Zone (Sardinia, Italy). *Journal of Structural Geology*, 66, 188-204. doi: 10.1016/j.jsg.2014.05.016
9. Casini, L., Oggiano, G. (2008). Late orogenic collapse and thermal doming in the northern Gondwana margin incorporated in the Variscan Chain: a case study from the Ozieri Metamorphic Complex, northern Sardinia, Italy. *Gondwana Research*, 13, 396-406.
10. Casini, L., Cuccuru, S., Maino, M., Oggiano, G., Tiepolo, M. (2012). Emplacement of the Arzachena pluton (Corsica-Sardinia batholith) and the geodynamics of the incoming Pangea. *Tectonophysics*, 544–545, 31–49. doi.org/10.1016/j.tecto.2012.03.028.
11. Casini, L., Cuccuru, S., Maino, M., Oggiano, G., Puccini, A., Rossi, P. (2015a). Structural map of Variscan northern Sardinia (Italy). *Journal of Maps*, 11(1), 75-84. doi: 10.1080/17445647.2014.936914.
12. Casini, L., Cuccuru, S., Puccini, A., Oggiano, G., Rossi, Ph. (2015b). Evolution of the Corsica–Sardinia batholith and late-orogenic shearing of the Variscides. *Tectonophysics*, 646, 65–78. doi.org/10.1016/j.tecto.2015.01.017.
13. Clemens, J. D., Wall, J. V. (1981). Origin and crystallization of some peraluminous (S-type) granitic magmas. *Canadian Mineralogist*, 19, 111–131.
14. Cocherie, A., Rossi, Ph., Fouillac, A.M., Vidal, Ph. (1994). Crust and mantle contributions to granite genesis -an example from the Variscan batholith of Corsica, France, studied by trace element and Nd-Sr-O-isotope systematics. *Chemical Geology*, 115, 173–211. doi.org/10.1016/0009-2541(94)90186-4.
15. Cocherie, A., Rossi, P., Fanning, C. M., Guerrot, C. (2005). Comparative use of TIMS and SHRIMP for U–Pb zircon dating of A-type granites and mafic tholeiitic layered complexes and dykes from the Corsican Batholith (France). *Lithos*, 82, 185-219. doi: 10.1016/j.lithos.2004.12.016.
16. Conte, A. M., Cuccuru, S., D’Antonio, M., Naitza, S., Oggiano, G., Secchi, F., Casini, L., Cifelli, F. (2017). The post-collisional late Variscan ferroan granites of southern Sardinia (Italy): Inferences for inhomogeneity of lower crust. *Lithos*, 294–295, 263–282. doi.org/10.1016/j.lithos.2017.09.028.
17. Conte, A. M., Naitza, S., Oggiano, G., Secchi, F., Cuccuru, S., Casini, L., Puccini, A. (2018a). Architecture, emplacement mode of late-Variscan plutons and their relationships with post-collisional phases: examples from Sarrabus igneous massif (SE Sardinia, Italy). Abstract book Congresso congiunto SIMP-SGI, Catania, 12-14 settembre 2018. doi.org/10.3301/ABSGI/2018.02.
18. Conte, A. M., Cuccuru, S., D’Antonio, M., Naitza, S., Oggiano, G., Secchi, F. (2018b). Long-lasting mantle-derived activity and evolution in the late-Variscan Sàrrabus igneous complex (SE Sardinia, Italy). Abstract book Congresso congiunto SIMP-SGI, Catania, 12-14 settembre 2018. doi.org/10.3301/ABSGI/2018.02.

- 721 19. Cortesogno, L., Cassinis, G., Dallagiovanna, G., Gaggero, L., Oggiano, G., Ronchi, a., Seno, S.,
722 Vsnossi, M. (1998). The Variscan post-collisional volcanism in Late Carboniferous–Permian
723 sequences of Ligurian Alps, Southern Alps and Sardinia (Italy): a synthesis. *Lithos*, 45, 305-328.
724 [https://doi.org/10.1016/S0024-4937\(98\)00037-1](https://doi.org/10.1016/S0024-4937(98)00037-1).
- 725 20. Cruciani, G., Franceschelli, M., Groppo C., Oggiano, G., Spano, M. E. (2015)- Re-equilibration
726 history and P–T path of eclogites from Variscan Sardinia, Italy: a case study from the medium-grade
727 metamorphic complex. *International Journal of Earth Sciences*, 104, 797–814.
- 728 21. Cuccuru, S., Naitza, S., Secchi, F., Puccini, A., Casini, L., Pavanetto, P., Linnemann, U., Hofmann
729 M., Oggiano, G. (2016). Structural and metallogenic map of late Variscan Arbus igneous complex
730 (SW Sardinia, Italy). *Journal of maps*, 12, 860–865.
- 731 22. Dack, A.V. (2009). Internal Structure and Geochronology of the Gerrei Unit in the Flumendosa Area,
732 Variscan External Nappe Zone, Sardinia, Italy. M. A. Thesis., Boise State University. Idaho, USA.
- 733 23. Dahlquist, J.A., Galindo, C., Pankhurst, R.J., Rapela, C.W., Alasino, P.H., Saavedra, J., Fanning, C.M.
734 (2007). Magmatic evolution of the Peñón Rosado granite: Petrogenesis of garnet-bearing granitoids.
735 *Lithos*, 95, 177-207.
- 736 24. D'Angelo, R. (1998). Rilevamento e caratterizzazione petrografica delle masse basiche del settore
737 Geremèas-Monte Turnu (Sàrrabus, Sardegna sud-orientale). M.Sc. Thesis. Università degli Studi di
738 Cagliari. 1-127.
- 739 25. DePaolo, D. J., Wasserburg, G. J. (1976). Nd isotopic variations and petrogenetic models. *Geophysical*
740 *Research Letters*, 3, 249–252. <https://doi.org/10.1029/GL003i005p00249>.
- 741 26. DePaolo, D. J., Perry, F. V., Baldrige, W. S. (1992). Crustal versus mantle sources of granitic
742 magmas: a two-parameter model based on Nd isotopic studies. *Transactions of the Royal Society of*
743 *Edinburgh: Earth Sciences*, 83, 439–446.
- 744 27. Dini, A., Di Vincenzo, G., Ruggieri, G., Rayner, J., Lattanzi, P. (2005). Monte Ollasteddu, a new gold
745 discovery in the Variscan basement of Sardinia (Italy): first isotopic (^{40}Ar – ^{39}Ar , Pb) and fluid
746 inclusion data. *Mineralium Deposita*, 40, 337–346.
- 747 28. Di Vincenzo, G., Andriessen, P. A., Ghezzi, C. (1996). Evidence of Two Different Components in a
748 Hercynian Peraluminous cordierite bearing granite: the San Basilio Intrusion (Central Sardinia, Italy).
749 *Journal of Petrology*, 37, 1175-1206. doi.org/10.1093/petrology/37.5.1175.
- 750 29. Downes, H. and Leyreloup, A. F. (1986). Granulitic xenoliths from the French Massif Central:
751 petrology, Sr and Nd isotope systematic and model ages estimates. *Geological Society London Special*
752 *Publications*, 24, 319–330.
- 753 30. Downes, H., Shaw, A., Williamson, B.J., Thirlwall, M. F. (1997). Sr, Nd and Pb isotopic evidence for
754 the lower crustal origin of Hercynian granodiorites and monzogranites, Massif Central, France.
755 *Chemical Geology*, 136, 99–122.
- 756 31. Edel, J. B., Casini, L., Oggiano, G., Rossi, P., Schulmann, K. (2014). Early Permian 90° clockwise
757 rotation of the Maures–Esterel–Corsica–Sardinia block confirmed by new palaeomagnetic data and
758 followed by a Triassic 60° clockwise rotation. *Geological Society London Special Publications*, 405,
759 333–361. doi: 10.1144/SP405.10.
- 760 32. Edel, J. B., Schulmann, K., Lexa, O., Diraison, M., Géraud, Y. (2015). Permian clockwise rotations
761 of the Ebro and Corso-Sardinian blocks during Iberian–Armorican oroclinal bending: Preliminary
762 paleomagnetic data from the Catalan Coastal Range (NE Spain). *Tectonophysics*, 657, 172-186.
- 763 33. Ferré, E. C. and Leake, B. E. (2001). Geodynamic significance of early orogenic high-K crustal and
764 mantle melts: example of the Corsica Batholith. *Lithos*, 59(1-2), 47-67. doi: 10.1016/s0024-
765 4937(01)00060-3.
- 766 34. Franciosi, L., D'Antonio, M., Fedele, L., Guarino, V., Tassinari, C. C. G., de Gennaro, R., Cucciniello,
767 C. (2019). Petrogenesis of the Solanas gabbro-granodiorite intrusion, Sàrrabus (southeastern Sardinia,
768 Italy): implications for Late Variscan magmatism. *International Journal of Earth Sciences*, 108, 989-
769 1012. DOI: 10.1007/s00531-019-01689-8.
- 770 35. Franzini, M., Leoni, L., Saitta, M. A. (1972). A simple method to evaluate the matrix effects in X-ray
771 fluorescence analysis. *X-Ray Spectrometry*, 1 (4), 151–154.
- 772 36. Frost, B. R., Barnes, C. G., Collins, W. J., Arculus, R. J., Ellis, D. J., Frost, C. D. (2001). A geochemical
773 classification for granitic rocks. *Journal of Petrology*, 42, 2033–2048.
- 774 37. Funedda, A., Naitza, S., Butta, C., Cocco, F., Dini, A. (2018). Structural controls of ore mineralization
775 in a polydeformed basement: field examples from the Variscan Baccu Locci shear zone (SE Sardinia,
776 Italy). *Minerals*, 8(10), 456. <https://doi.org/10.3390/min8100456>

- 777 38. Gaggero, L., Oggiano, G., Buzzi, L., Slejko, F., Cortesogno, F. (2007). Post-Variscan mafic dikes from
778 the late orogenic collapse to the Tethyan rift: evidence from Sardinia. *Ofioliti*, 32, 15–37.
- 779 39. Gaggero, L., Oggiano, G., Funedda, A., Buzzi, L. (2012). Rifting and arc-related early Paleozoic
780 volcanism along the north Gondwana margin: geochemical and geological evidence from Sardinia
781 (Italy) *The Journal of Geology*, 120, 273-292. <https://doi.org/10.1086/664776>
- 782 40. Gaggero, L., Gretter, N., Langone, A., Ronchi, A. (2017). U–Pb geochronology and geochemistry of
783 late Palaeozoic volcanism in Sardinia (southern Variscides). *Geoscience Frontiers*, 8, 1263-1284.
784 <https://doi.org/10.1016/j.gsf.2016.11.015>.
- 785 41. Giovanardi, T. and Lugli, F. (2017). The Hf-INATOR: A free data reduction spreadsheet for Lu/Hf
786 isotope analysis. *Earth Science information*, 10, 517–523.
- 787 42. Giovanardi, T.; Mazzucchelli, M.; Lugli, F.; Girardi, V.A.; Correia, C.; Tassinari, C.C.; Cipriani, A.
788 (2018) Isotopic constraints on contamination processes in the Tonian Goiás Stratiform Complex.
789 *Lithos*, 310, 136–152.
- 790 43. Green, T.H. (1977). Garnet in silicic liquids and its possible use as a P-T indicator. *Contributions to*
791 *Mineralogy and Petrology* 65, 59-67.
- 792 44. Hart, S.R., Blusztajn, J., Dick, H.J.B., Meyer, P.S., Muehlenbachs, K. (1999). The fingerprint of
793 seawater circulation in a 500-meter section of ocean crust gabbros. *Geochimica et Cosmochimica Acta*,
794 63, 4059–4080.
- 795 45. Hodkinson, D., Krogstadt, E. J., Brown, M. (1995). Geochemical constraints on magma sources of
796 Mesozoic continental arc plutonic complexes, Andean plate boundary zone, North Chile. In *The origin*
797 *of granites and related rocks. Third Hutton. Symposium*, College Park, M. D,66-67.
- 798 46. Janoušek, V., Rogers, G., Bowes, D.R. (1995). Sr-Nd isotopic constraints on the petrogenesis of the
799 Central Bohemian Pluton, Czech Republic. *Geologische Rundschau*, 84, 520–534.
- 800 47. Janoušek, V., Moyen, J. F., Martin, H., Erban, V., & Farrow, C. (2016). Geochemical modelling of
801 igneous processes: principles and recipes in R language. *Bringing the Power of R to a Geochemical*
802 *Community*. Springer-Verlag, Berlin, Heidelberg. ISBN 978-3-662-46792-3.
- 803 48. Kröner, A. Willner, P. (1998). Time of formation and peak of Variscan HP-HT metamorphism of
804 quartz-feldspar rocks in the central Erzgebirge, Saxony, Germany. *Contributions to Mineralogy and*
805 *Petrology*, 132, 1–20.
- 806 49. Lu, S., Zhu, X., Li, X. (2019). Geochronology and geochemistry of the five magmatic rocks in the
807 Ningzhen region, China. *Acta Geochimica*, 38(02), 241-261. [https://doi.org/10.1007/s11631-019-](https://doi.org/10.1007/s11631-019-00316-2)
808 [00316-2](https://doi.org/10.1007/s11631-019-00316-2).
- 809 50. Ludwig, K. R. (2012). *Isoplot 3.75. A geochronological toolkit for Microsoft Excel*. Berkeley
810 *Geochronology Center. Special publication*, 5.
- 811 51. Matte, P. (2001). The Variscan collage and orogeny (480-290 Ma) and the tectonic definition of the
812 Armorica microplate. *Terra Nova*, 13, 122-128.
- 813 52. McDonough, W. F., Sun, S.S. (1995). The composition of the Earth. *Chemical Geology*, 120, 223–
814 253.
- 815 53. Meloni, M. A., Oggiano, G., Funedda, A., Pistis, M., Linnemann, U. (2017). Tectonics, ore bodies,
816 and gamma-ray logging of the Variscan basement, southern Gennargentu massif (Central Sardinia,
817 Italy). *Journal of maps*, 13, 196–206.
- 818 54. Miller, C. F. (1985). Are strongly peraluminous magmas derived from pelitic sedimentary sources?
819 *Journal of Geology*, 93, 673–689.
- 820 55. Musumeci, G., Spano, M. E., Cherchi, G. P., Franceschelli, M., Pertusati, P. C., Cruciani, G. (2014).
821 Geological Map of the Monte Grighini Variscan Complex (Sardinia, Italy). *Journal of Maps*, 287-298
822 <https://doi.org/10.1080/17445647.2014.924441>.
- 823 56. Naitza, S., Conte, A.M., Cuccuru, S., Oggiano, G., Secchi, F., Tecce, F. (2017). A Late Variscan tin
824 province associated to the ilmenite-series granites of the Sardinian Batholith (Italy): the Sn and Mo
825 mineralisation around the Monte Linas ferroan granite. *Ore Geology Reviews*, 80, 1259–1278.
- 826 57. Nicoletti, M., Ardanese L. R., Colasanti, S. (1982). La granodiorite di Capo Carbonara (Sardegna-
827 Italia). Età K-Ar di fasi minerali in paragenesi. *Rendiconti Società Italiana di Mineralogia e*
828 *Petrologia*, 38(2), 765-769.
- 829 58. Oggiano, G., Gaggero, L., Funedda, A., Buzzi, L., Tiepolo, M. (2010). Multiple early Paleozoic
830 volcanic events at the northern Gondwana margin: U–Pb age evidence from the Southern Variscan
831 branch (Sardinia, Italy). *Gondwana Research*, 17, 44–58.

- 832 59. Paquette, J. L., Ménot, R.-P., Pin, C., Orsini, J. B. (2003). Episodic and short-lived granitic pulses in
833 a post-collisional setting: evidence from precise U–Pb zircon dating through a crustal cross-section in
834 Corsica. *Chemical Geology*, 198 (1-2), 1-20. doi: 10.1016/s0009-2541(02)00401-1.
- 835 60. Pirinu, N. (1994). Le sieniti del Sàrrabus meridionale (Sardegna SE). Unpublished PhD thesis,
836 University of Napoli. 1-81.
- 837 61. Poli, G., Ghezzi, C., Conticelli, S. (1989). Geochemistry of granitic rocks from the Hercynian
838 Sardinia-Corsica batholith: Implication for magma genesis. *Lithos*, 23(4), 247-266. doi:
839 10.1016/0024-4937(89)90038-8.
- 840 62. Poli, G., Tommasini, S. (1999). Geochemical modelling of acid-basic magma interaction in the
841 Sardinia-Corsica Batholith: the case study of Sàrrabus, southeastern Sardinia, Italy. *Lithos* 46, 553-
842 571.
- 843 63. Puccini, A., Xhixha, G., Cuccuru, S., Oggiano, G., Kaçeli Xhixha, M., Mantovani, F., Rossi Alvarez,
844 C., Casini, L. (2013). Radiogenic heat potential of the Sardinian Variscan crust. *Goldschmidt 2013*
845 *Conference Abstracts*. 2002
- 846 64. Renna, M. R., Tribuzio, R., Tiepolo, M. (2006). Interaction between basic and acid magmas during
847 the latest stages of the post-collisional Variscan evolution: clues from the gabbro–granite association
848 of Ota (Corsica–Sardinia batholith). *Lithos*, 90, 92–110. doi:10.1016/j.lithos.2006.02.003.
- 849 65. Ronca, S., Del Moro, A., Traversa, G. (1999). Geochronology, Sr-Nd isotope geochemistry and
850 petrology of Late Hercynian dike magmatism from Sarrabus (SE Sardinia). *Periodico di Mineralogia*,
851 68, 231–260.
- 852 66. Rossi, Ph., Cocherie, A. (1991). Genesis of a Variscan batholith: field, petrological and mineralogical
853 evidence from the Corsica-Sardinia batholith. *Tectonophysics*, 195, 319–346.
- 854 67. Rossi, Ph., Oggiano, G., Cocherie, A. (2009). A restored section of the “southern Variscan realm”
855 across the Corsica–Sardinia microcontinent. *Comptes Rendus Geoscience* 341, 224–238.
- 856 68. Rossi, Ph., Cocherie, A., Fanning, C. M. (2015). Evidence in Variscan Corsica of a brief and
857 voluminous Late Carboniferous to Early Permian volcanic-plutonic event contemporaneous with a
858 high-temperature/low-pressure metamorphic peak in the lower crust. *Bulletin de la Société Géologique*
859 *de France*, 186, 171–192. doi.org/10.2113/gssgfbull.186.2-3.171.
- 860 69. Secchi, F., Brotzu, P., Callegari, E. (1991). The Arburèse igneous complex (SW Sardinia, Italy) –an
861 example of dominant igneous fractionation leading to peraluminous cordierite-bearing leucogranites
862 as residual melts. In: A. Peccerillo (Ed.), *Geochemistry of granitoid Rocks*. *Chemical Geology*, 92,
863 213–249.
- 864 70. Secchi, F., Naitza, S., Oggiano, G., Cuccuru, S., Puccini, A., Conte, A. M., Giovanardi, T.,
865 Mazzucchelli, M., 2021. Geology of late-Variscan Sàrrabus pluton (south-eastern Sardinia, Italy).
866 *Journal of maps*. 17, <https://doi.org/10.1080/17445647.2021.1982032>.
- 867 71. Shirey, S. B., Hanson, G. N. (1986). Mantle heterogeneity and crustal recycling in Archean granite-
868 greenstone belts: evidence from Nd isotopes and trace elements in the Rainy Lake area, Superior
869 Province, Ontario, Canada. *Geochimica et Cosmochimica Acta*, 50, 2631–2651.
870 [https://doi.org/10.1016/0016-7037\(86\)90215-2](https://doi.org/10.1016/0016-7037(86)90215-2)
- 871 72. Stampfli, G. M., von Raumer, J., Borel, G. (2002). The paleozoic evolution of pre-Variscan terranes:
872 From Gondwana to the Variscan collision. *Geological Society of America*, 364, 263–280.
- 873 73. Stormer, J. C., Nicholls, J., 1978. XLFRAC: a program for the interactive testing of magmatic
874 differentiation models. *Computers and Geosciences* 4, 143–159.
- 875 74. Thirwall, M. F. (1991). Long-term reproducibility of multicollector Sr and Nd isotope ratio analysis 1.
876 *Chemical Geology*, 94, 85-104. [https://doi.org/10.1016/S0009-2541\(10\)80021-X](https://doi.org/10.1016/S0009-2541(10)80021-X)
- 877 75. Tommasini, S., Poli, G. (1992). Petrology of the late-Carboniferous Punta Falcone gabbroic complex,
878 northern Sardinia, Italy. *Contribution to Mineralogy and Petrology*, 110, 16–32.
- 879 76. Tommasini, S., Poli, G., Halliday, A. N. (1995). The role of sediment subduction and crustal growth
880 in Hercynian plutonism: isotopic and trace element evidence from the Sardinia–Corsica Batholith. *J.*
881 *Petrol.* 36, 1305–1332.
- 882 77. Villaseca, C., Barbero, L., Rogers, G. (1998). Crustal origin of Hercynian peraluminous granitic
883 batholiths of Central Spain: petrological, geochemical and isotopic (Sr, Nd) constraints. *Lithos*, 43,
884 55–79.
- 885 78. Villaseca, C., Pérez-Soba, C., Merino, E. M., Orejana, D., López-García, J. A., Billstrom, K. (2008)
886 *Contrasted crustal sources for peraluminous granites of the segmented Montes de Toledo Batholith*

- 887 (Iberian Variscan Belt). *Journal of Geosciences*, 53, 263–280. DOI:
888 <http://dx.doi.org/10.3190/jgeosci.035>
889 79. Woodhead, J.D. and Hergt, J.M. (2005), A Preliminary Appraisal of Seven Natural Zircon Reference
890 Materials for In Situ Hf Isotope Determination. *Geostandards and Geoanalytical Research*, 29: 183-
891 195. <https://doi.org/10.1111/j.1751-908X.2005.tb00891.x>
892 80. Zorpi, M. J., Coulon, C., Orsini, J. B. (1991). Hybridization between felsic and mafic magmas in
893 calcalkaline granitoids a case study in northern Sardinia, Italy. *Chemical Geology*, 92, 45-86.
894

895

896

897 Figure Captions

898

899 Fig. 1: simplified geological map of Sardinia-Corsica batholith (after Casini et al., 2012). 1-4:
900 metamorphic basement. (1) Pan-African schists. (2) Unmetamorphosed Foreland. (3) Low- to
901 medium-grade metamorphic units (nappe zone). (4) High grade metamorphic complex. 5-6 Sardinia-
902 Corsica batholith. (5) Syn-collisional Variscan magmatism (Mg-K rock-series). (6) Late-Variscan
903 post-collisional magmatism. (7) Post-Variscan covers. Other symbols: main Variscan faults (8). From
904 north to south, Arg, SM, Arz, Br, Gn, Gh, Arb and SV refer to localities cited in the text (Santa Maria
905 Island, Arzachena, Barrabisa, Gennargentu, Grighini, Arburèse and San Vito, respectively).
906

907 Fig. 2: Geological sketch map of late-Variscan Sàrrabus pluton (SE Sardinia, Italy). (1)
908 Undifferentiated epimetamorphic complex: metasandstones, metapelites and metalimestones
909 (Cambrian-early Carboniferous). (2-8) Late-Variscan igneous units of Sàrrabus pluton: (2) Two-
910 pyroxene biotite gabbro tonalites (Burcèi Unit). (3) biotite to biotite hornblende granodiorites (Cala
911 Regina Group) with syn-plutonic stocks and dismembered dikes of two pyroxene-bearing hornblende
912 gabbroic varieties (Solànas complex; SO). (4) Garnet-bearing two mica granites (Monte Maria Unit).
913 (5) biotite monzogranites grading to leucogranites (Brunco Nicola Bove Unit). (6) F-rich biotite
914 leucogranite (San Priamo Unit). (7) F-rich hastingsite granite stocks (Monte Sette Fratelli Unit). (8)
915 Mafic and acidic dike swarms. (9) Post-Mesozoic sedimentary and volcanic covers and recent
916 continental and transitional sedimentary deposits. Other symbols (10-12). Late-Variscan southern
917 Sàrrabus shear zone (SSSZ) (10). Main extensional faults, certain (11) and inferred/buried (12). CR,
918 Ge, TF, So, SC, Vs, Ca, S.P., Bu, S.G. and M. SF refer to Cala Regina, Geremèas, Torre de su Fenugu,
919 Solànas, Scala Carbonara, Villasimius, Castiadas, San Priamo, Burcei, San Gregorio and Monte Sette
920 Fratelli localities cited in the text, respectively.
921

922 Fig. 3: Field relationships of Sàrrabus igneous rocks. (a) Sub-horizontal magmatic foliation of
923 hornblende granodiorites evidenced by dark and felsic enclaves (FE; Capo Carbonara). (b) strongly
924 foliated quartz diorites with large mafic enclaves of quartz gabbroic composition (Porto Murròni); (c)
925 densely interdigitation between gabbroic rocks and quartz diorites (western slope of Torre de su
926 Fenùgu); (d) disrupted large syn-magmatic mafic dikes into granodiorite (western slope of Torre de
927 su Fenùgu); (e) contact relationships between different dike generation: composite dikes predate
928 metaluminous acidic dikes (Cala Regina); (f) fine-grained centimetric rounded dark enclaves in acidic
929 dike (Porto Murròni).
930

931 Fig. 4: Petrographical characters of magmatic rocks from Sàrrabus igneous massif. (a) two pyroxene-
932 bearing equigranular gabbroic rocks from inner part of Scala Carbonara body (crossed polars; Scala
933 Carbonara, sample SSP16.); (b) panidiomorphic textures of quartz microgabbros (crossed polars;
934 sample SSP17; Capo Carbonara); (c) cumulophyric texture of olivine-bearing dark layers from
935 stratified septa (crossed polars; Cabu Oi, sample SSP29); (d) clinopyroxene/brown amphibole
936 relationships in equigranular varieties of mafic dike (crossed polars; north of Olia Speciosa, sample
937 ESP10); (e) local plagioclase enriched zones in hornblende quartz diorites (crossed polars; sample

938 SSP8, Porto Murroni; (f) large patchy-zoned plagioclase lath on Cala Regina granodiorites (crossed
939 polars; Monte Nai, sample ESP1); (g) interstitial white mica in San Priamo leucogranites of (plane
940 polarized light; Monte Gruttas, sample SPP9); (h) Almandine garnet associated to pinitized cordierite
941 in peraluminous granites of Monte Maria Unit (plane polarized light; Porto Carbonara, sample LPC).
942

943 Fig. 5: Discrimination diagrams for the igneous rocks from Sàrrabus pluton. (a) Boundaries according
944 to Peccerillo and Taylor (1976); (b) discrimination diagram for basaltic rocks. HAB and HMB refer
945 to high alumina and high Mg basalts, respectively; boundaries according to Miyashiro (1974). (c) and
946 (d) Frost's and Frost (2001) discrimination diagrams. C, CA, AC and A refer calcic, calc-alkalic,
947 alkali-calcic and alkaline rock-series, respectively. Pale and smaller symbols refer to literature data.
948 Literature after Poli and Tommasini (1999) and Franciosi et al. (2019) is reported for comparison.
949 Fields refer to mafic and acidic dike swarms (data after Ronca et al., 1999).
950

951 Fig. 6: REE normalized patterns for Sàrrabus magmatism: (a) syn-plutonic gabbroic suite; solid,
952 double and dashed lines refer to olivine-bearing cumulate, two pyroxene-bearing gabbros and
953 hornblende Qz-gabbros, respectively. Light and pale blue fields refer to data for olivine-bearing
954 cumulates and hornblende Qz-gabbros (Franciosi et al., 2019), respectively. (b) Granodiorite rock-
955 association; solid, double and dashed lines refer to Qz-diorite, tonalitic granodiorite and foliated
956 granodiorite, respectively. The solid field refers to data for granodiorites after Franciosi et al. (2019);
957 (c) mafic dikes; solid field refers to data for basalts from Ronca et al. (1999); (d) granites and felsic
958 dikes; solid, dashed and dotted lines refer to peraluminous granite, metaluminous dikes and
959 peraluminous dike (data after Ronca et al., 1999), respectively. Dark and pale yellow solid fields refer
960 to San Priamo and Monte Sette Fratelli granites, respectively (data after Conte et al. (2017)). Data are
961 normalized to CI (Mc Donough and Sun, 1995). Labels in (c) as in Supplementary Material Table 1.
962

963 Fig. 7: Spider diagrams for syn-plutonic mafic (a) and granodiorite (b) rock-associations from
964 Sàrrabus pluton normalized to primitive mantle (McDonough and Sun, 1995). Peraluminous granite
965 is reported for comparison.
966

967 Fig. 8: $\epsilon\text{Nd}(t)$ vs. $^{87}\text{Sr}/^{86}\text{Sr}(t)$ for late-Variscan rocks from Sàrrabus pluton (south-eastern Sardinia,
968 Italy) calculated for an age of 286 Ma (see text). Red, orange, and blue colors refer to Corsica, Gallura
969 (northern Sardinia) and Sàrrabus pluton, respectively. Circle refer to peraluminous garnet-bearing
970 granite from Monte Maria Unit. Barred circles refer to metaluminous to sub-aluminous granites of
971 San Priamo and Monte Sette Fratelli units (data after Conte et al., 2017). Dike trend refers to mafic
972 to intermediate dikes from Sàrrabus pluton (data after Ronca et al., 1999). Data for Corsica mafic
973 suites after Cocherie et al. (1994); data for Gallura mafic suites after Tommasini et al., 1995 (Punta
974 Falcone) and Casini (Bortigiadas and La Etica), still unpublished data; mafic (subalkaline and
975 transitional) dikes after Gaggero et al., 2007). Dark blue arrow refers to gabbros to hornblende quartz
976 micro gabbros evolutive line (with olivin-cumulites at left hand). Note the position of granodiorites
977 outside of evolutive sequence and the intermediate position of tonalites for which a hybrid origin is
978 required. Note also that less evolved granodiorites (i.e., Scala Carbonara and Capo Carbonara) show
979 a more radiogenic character with respect of Solànas granodiorites (Porto Murroni).
980

981 Fig. 9: a) $f(\text{Sm}/\text{Nd})$ vs. NCI plot for the Sàrrabus pluton and other available Sardinia samples. $f(\text{Sm}/\text{Nd})$
982 $= (^{147}\text{Sm}/^{144}\text{Nd}_{\text{sample}})/(^{147}\text{Sm}/^{144}\text{Nd}_{\text{CHUR}}) - 1$ (DePaolo and Wasserburg, 1976); $\text{NCI} = [\epsilon\text{Nd}(\text{rock})$
983 $- \epsilon\text{Nd}(\text{MC})] / [\epsilon\text{Nd}(\text{CC}) - \epsilon\text{Nd}(\text{MC})]$ according DePaolo et al. (1992). Field refer to metasediments
984 from central-eastern Sardinia (data after Di Vincenzo et al., 1996). b) $f(\text{Sm}/\text{Nd})$ vs. $\epsilon\text{Nd}_{(286)}$ plot for
985 the Sàrrabus pluton and other available Sardinia sample. DM, EM and CC are according to Hodkinson
986 et al. (1995). Field refer to orthogneisses and migmatites from central-eastern Sardinia (data after Di
987 Vincenzo et al., 1996). Other symbols as in Fig. 5.
988

989 Fig. 10: Mixing binary plot of $^{87}\text{Sr}/^{86}\text{Sr}_{(286)}$ vs. $\epsilon\text{Nd}_{(286)}$ showing variability of rocks from Sàrrabus
990 pluton. Symbols as in Fig. 5 and 10; numbers refer to SSP samples reported in Supplementary
991 Material Table 3. Dashed lines refer to possible mixing hyperbolas obtained by reverse least-squares
992 method (Janoušek et al., 2016) using SSP6b (mafic dike) and SSP59 (peraluminous granite) samples
993 as mantle- and crustal-derived endmembers, respectively to model the observed granodiorite rock-
994 association. Pale field refer to data for granodiorite rock-association after Poli and Tommasini (1999)
995 and Franciosi et al. (2019).
996
997

Figure 1

[Click here to access/download;Figure;Figure 1.tif](#)

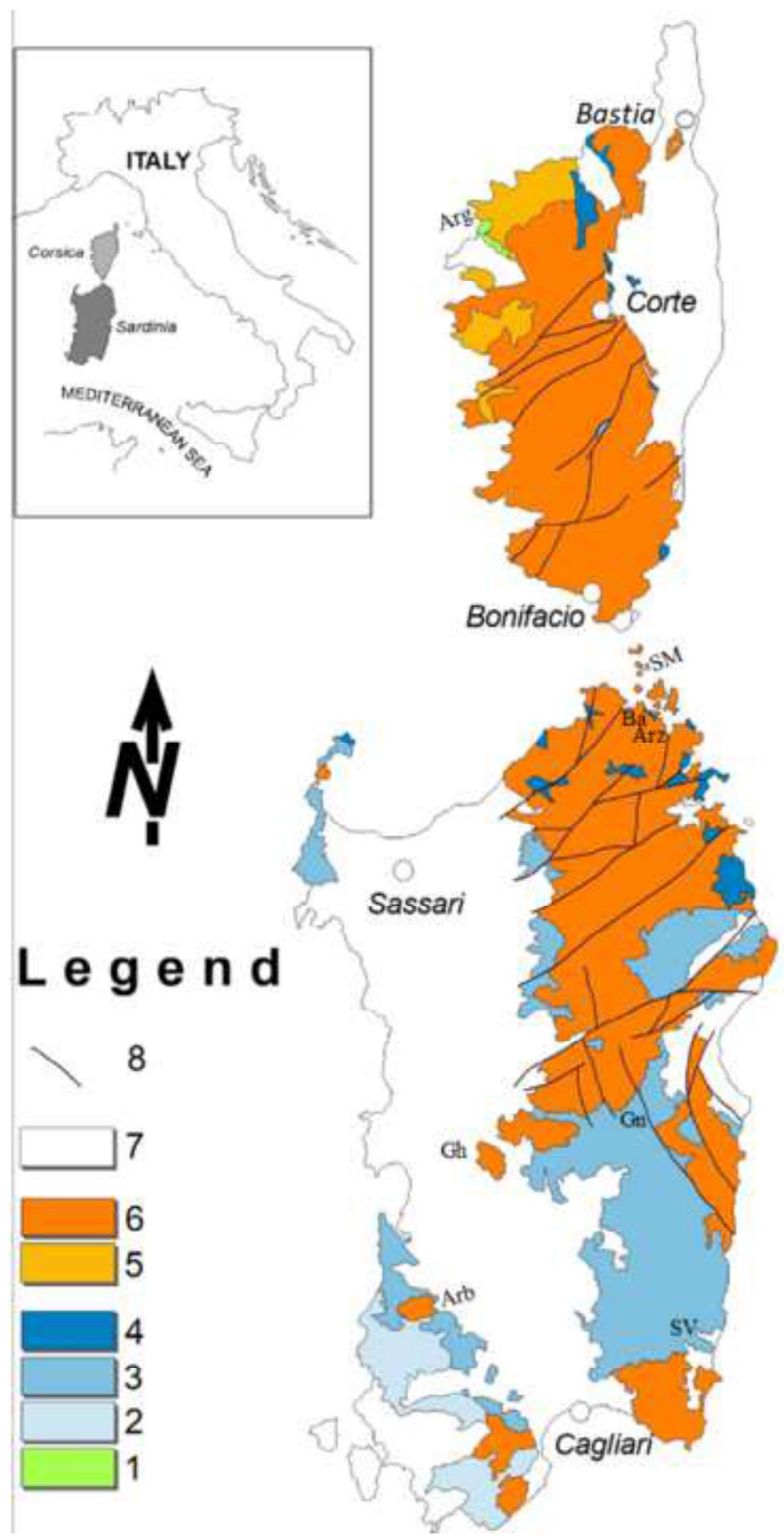
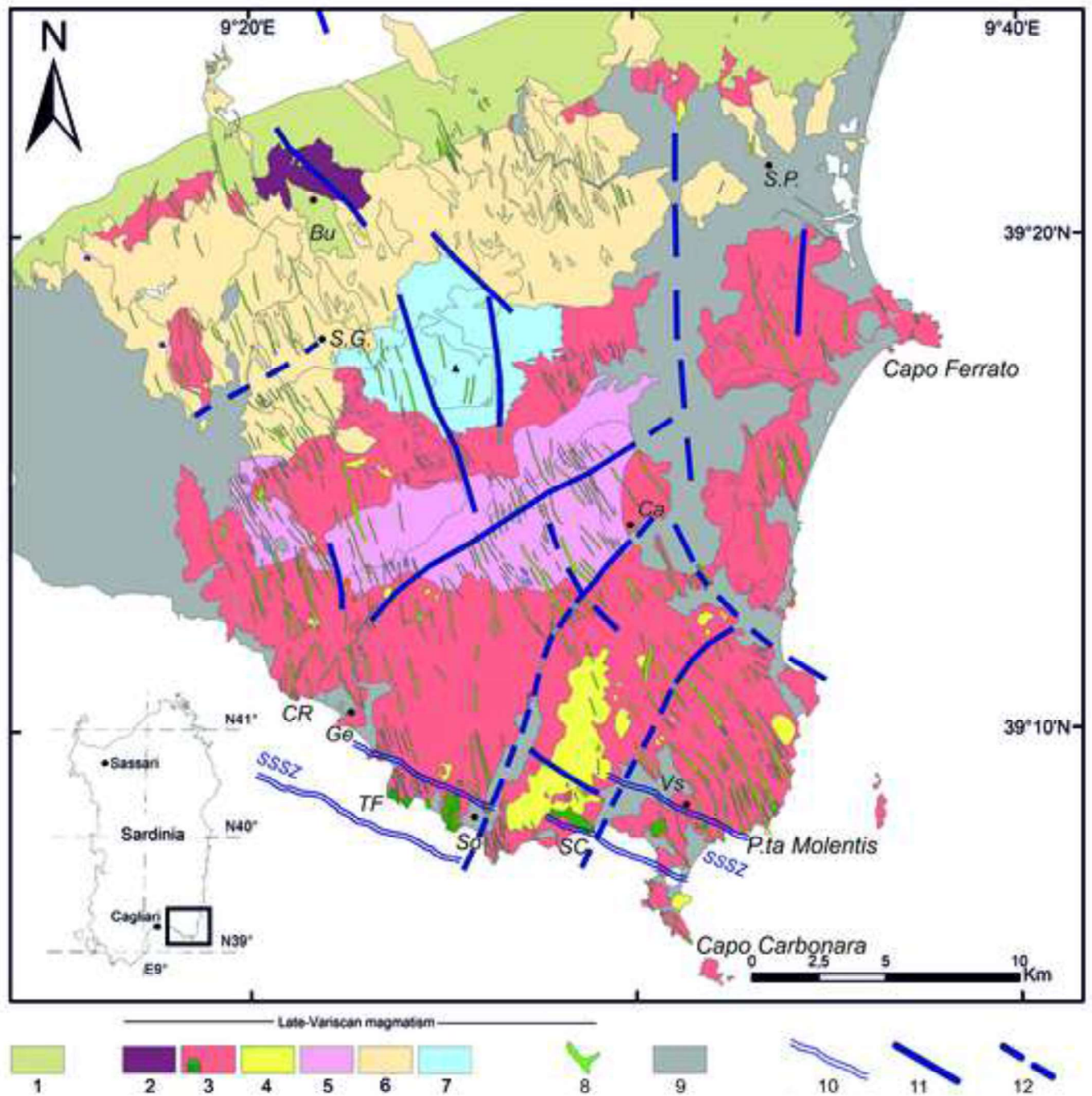


Figure 2

[Click here to access/download;Figure;Figure 2.jpg](#)



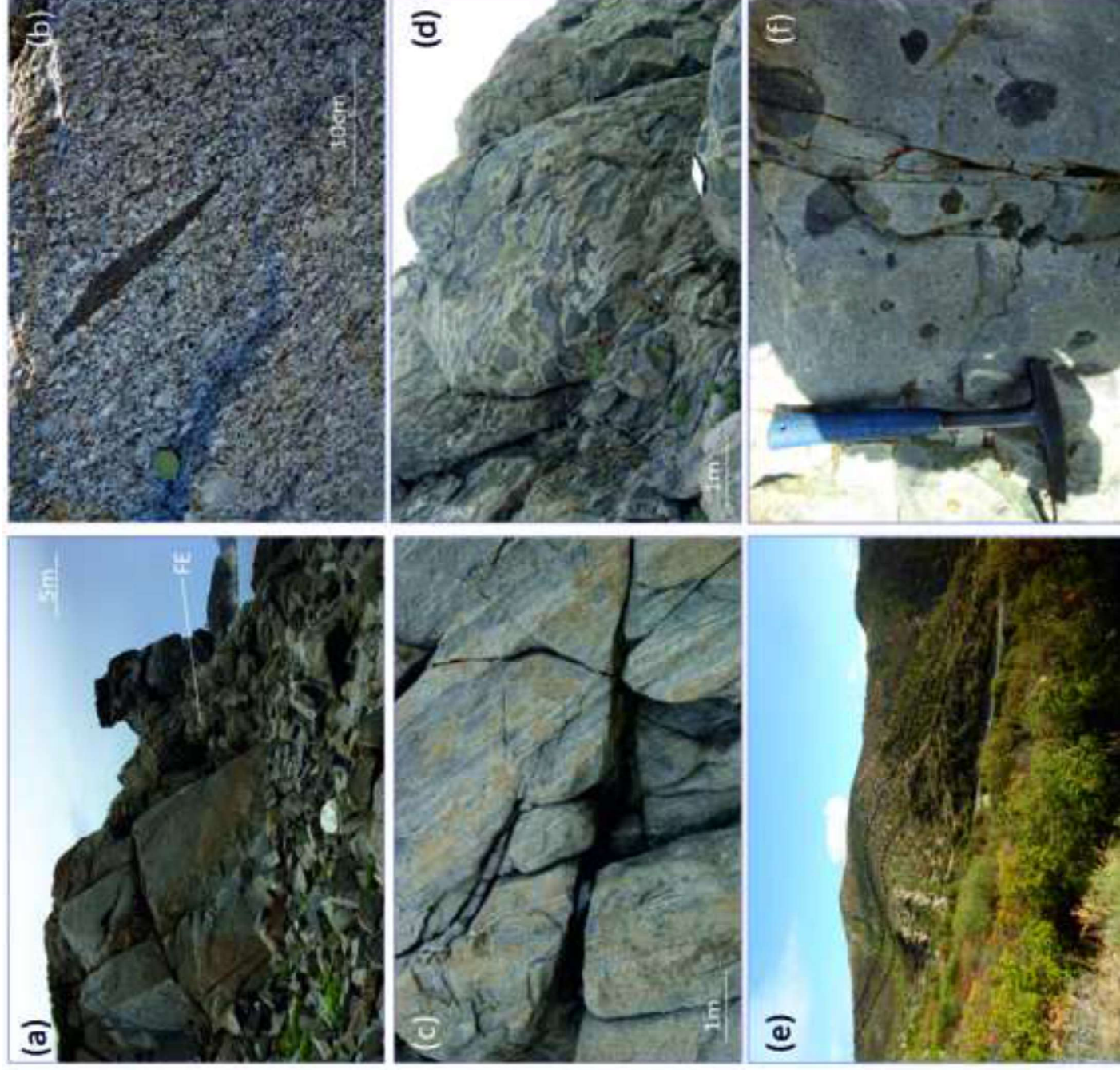
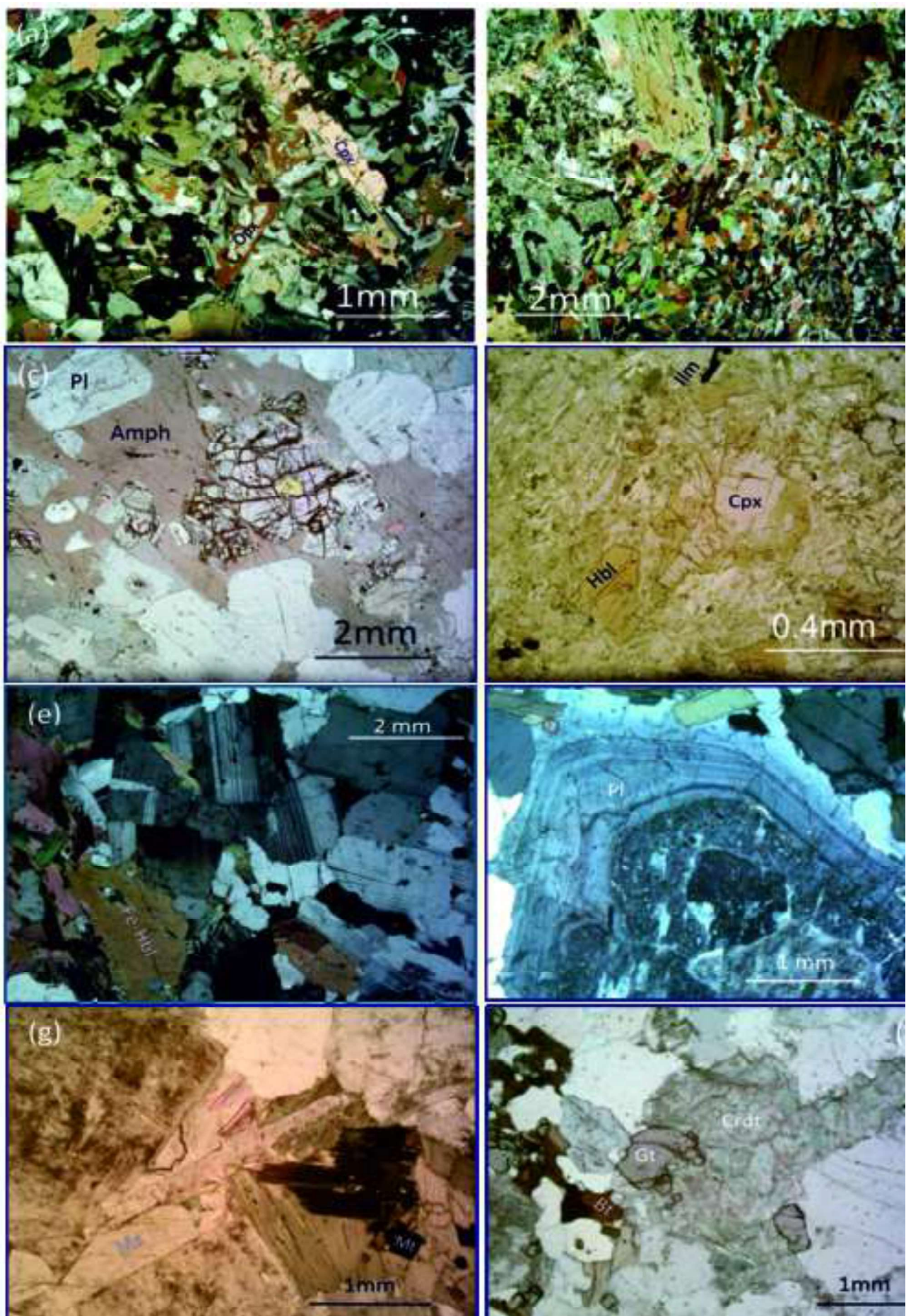
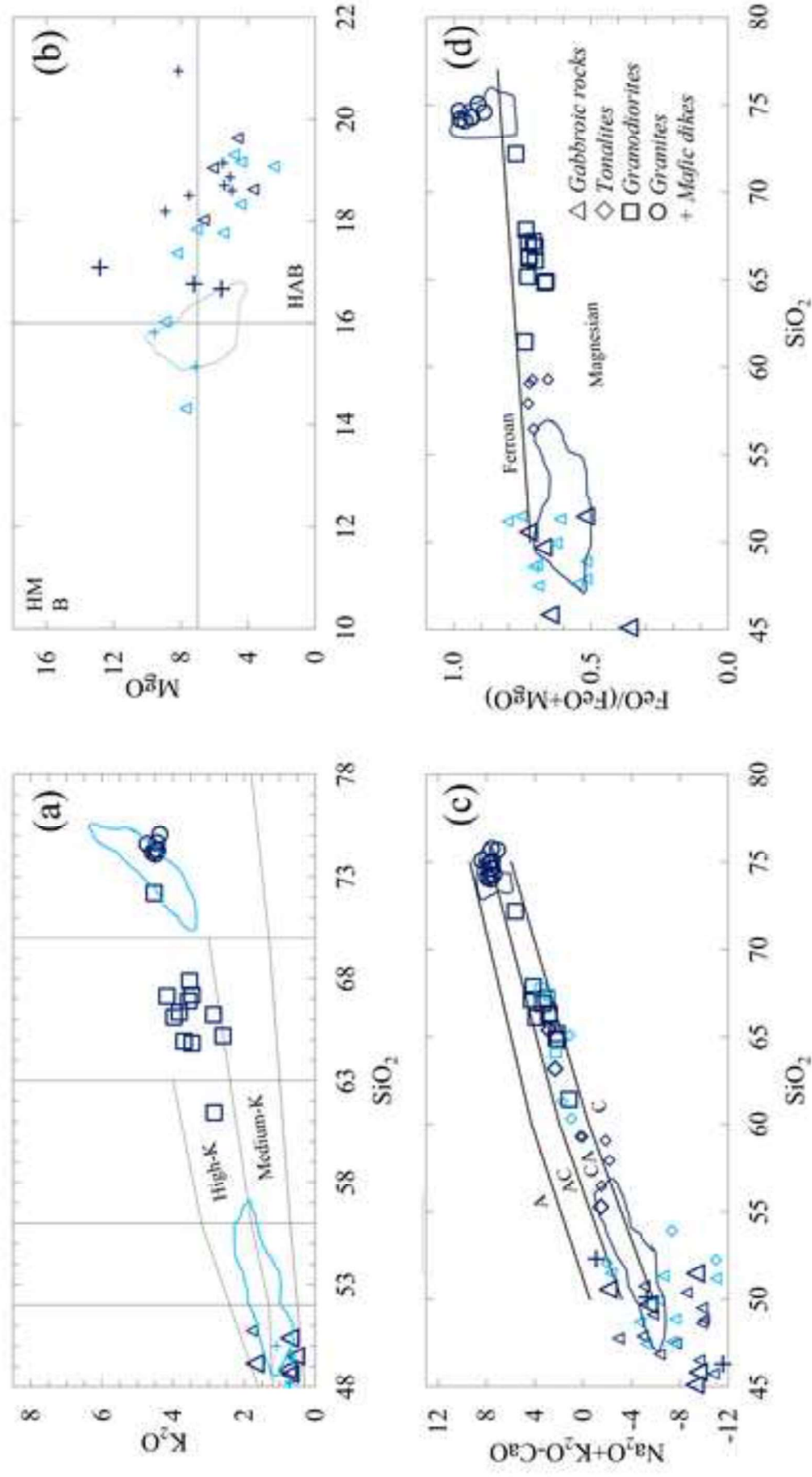


Figure 4

[Click here to access/download;Figure;Figure 4.tif](#)





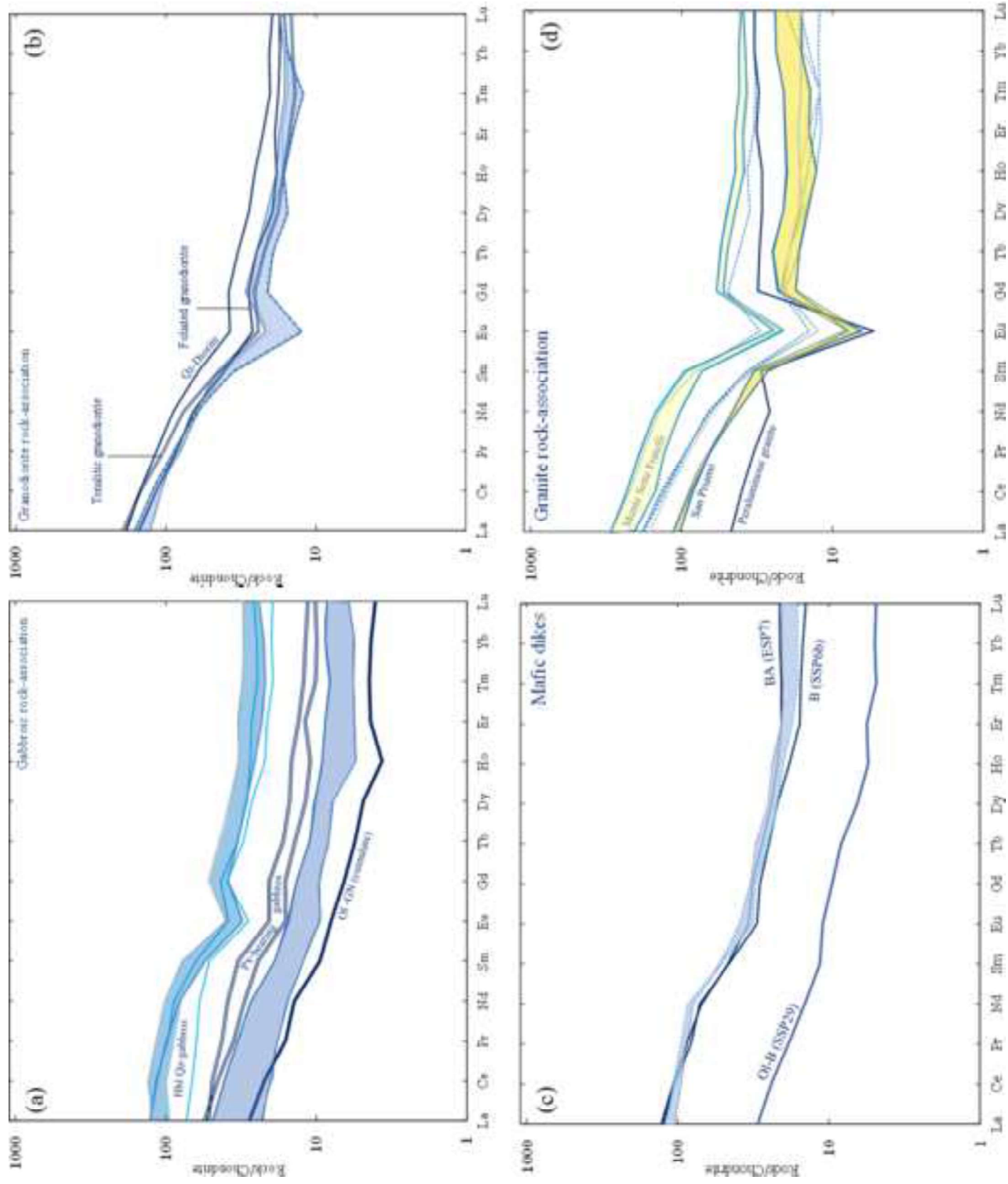
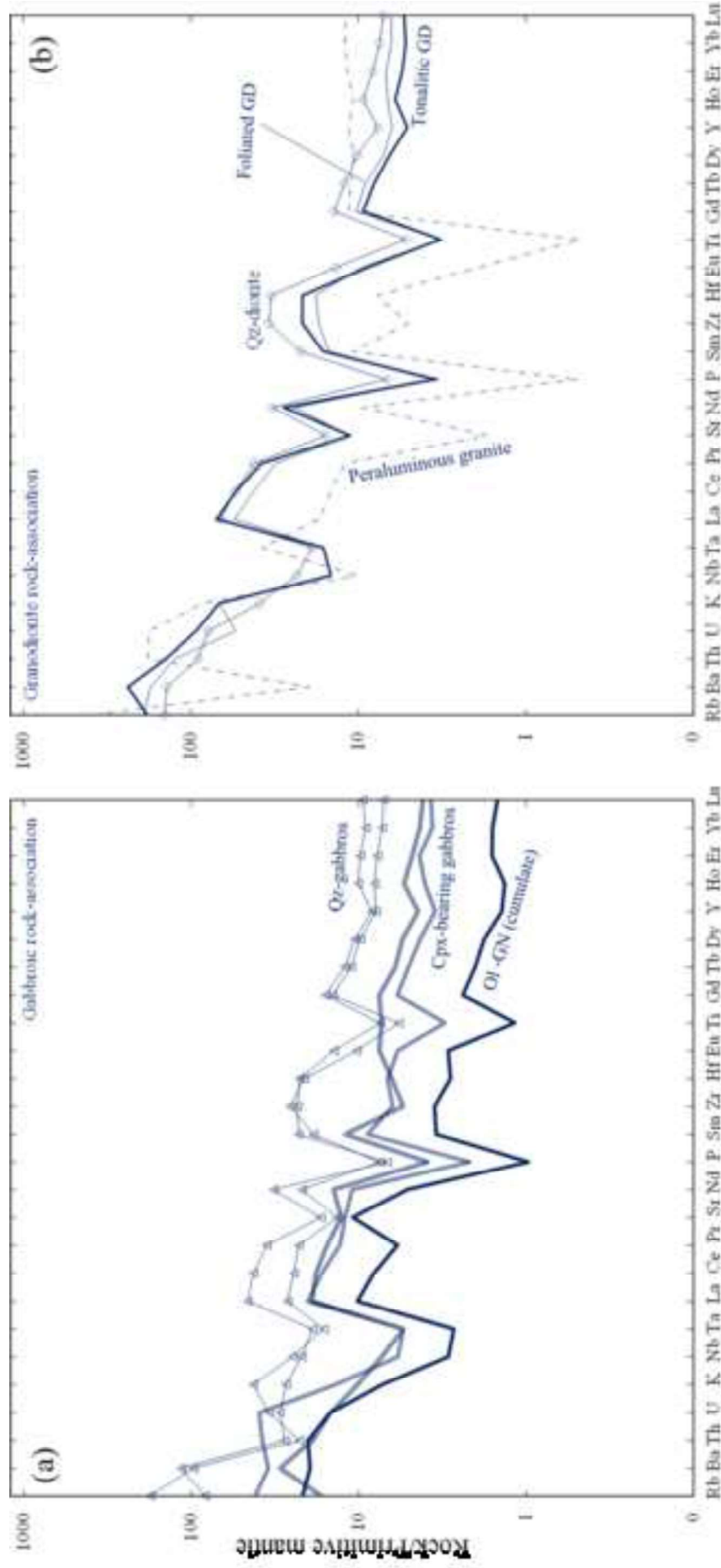
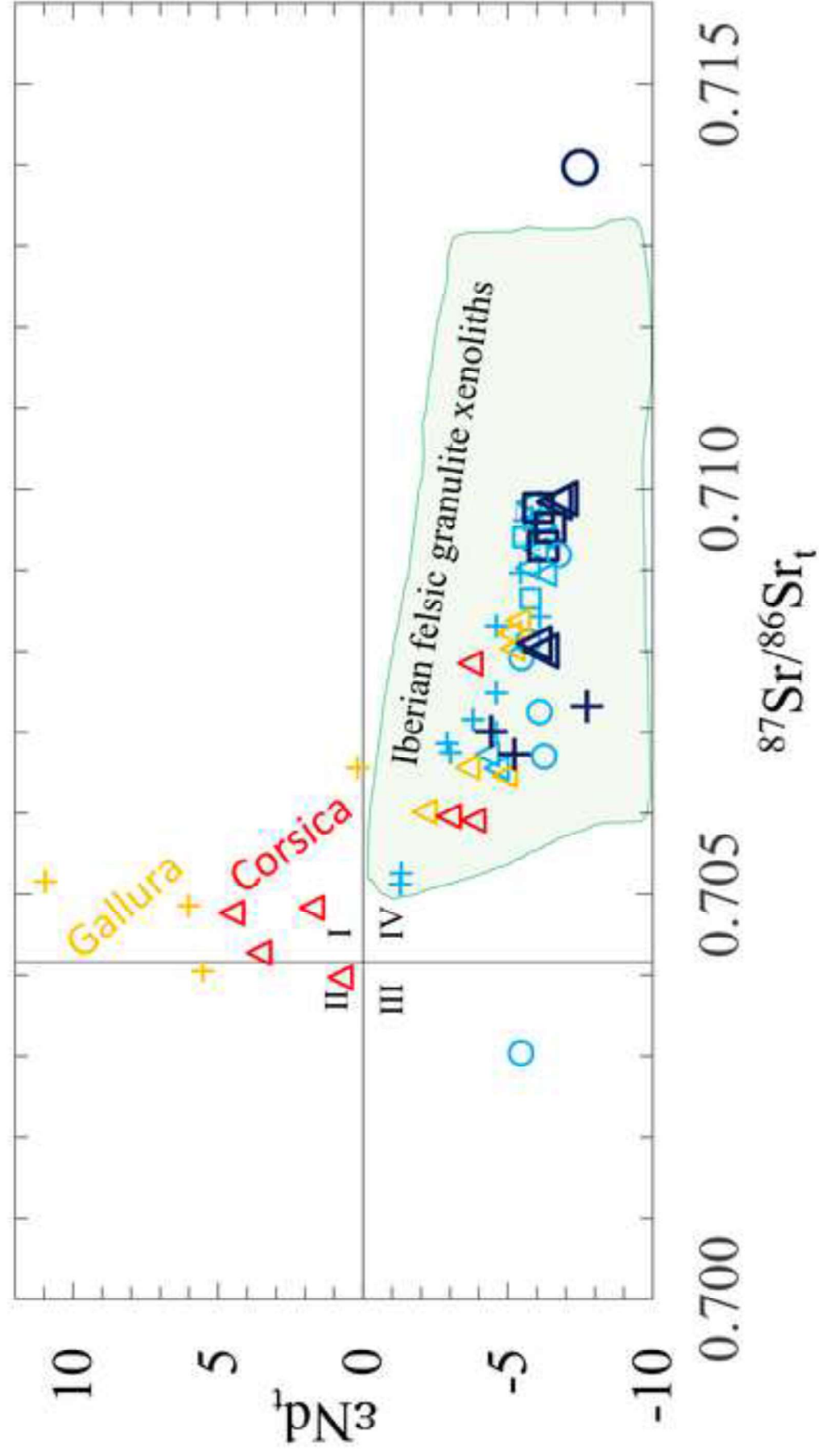
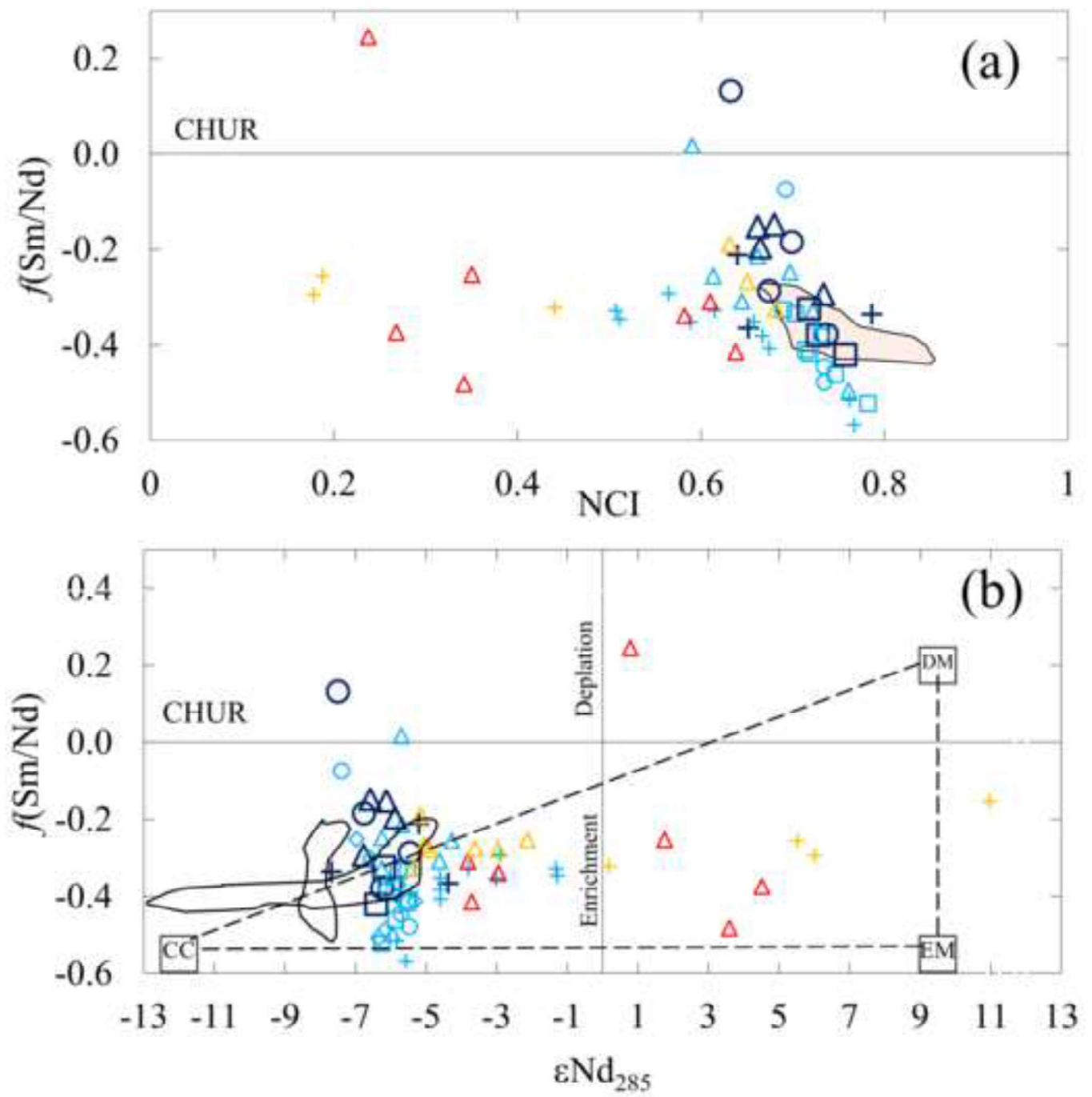
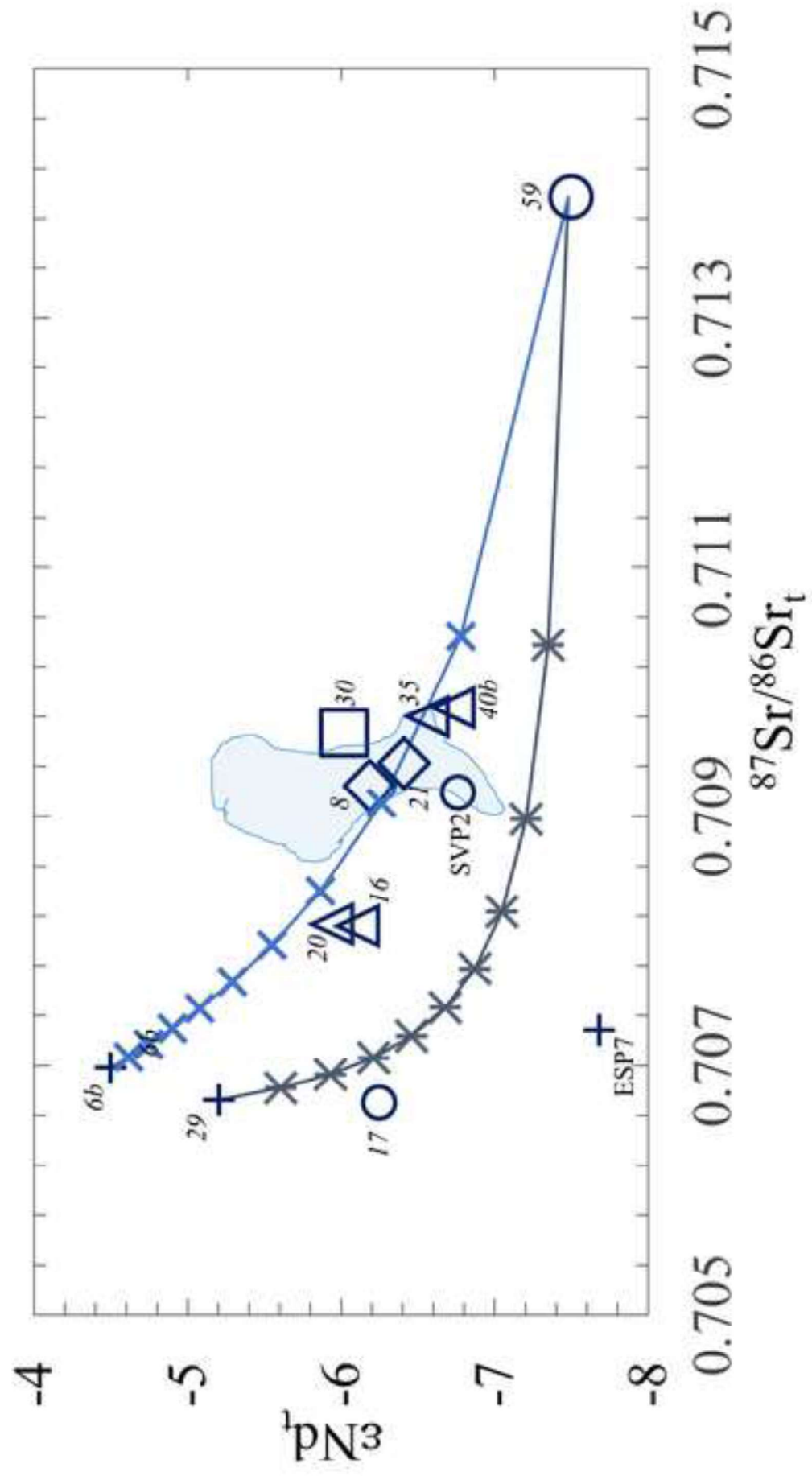


Figure 6









TABLES

Tab. 1 -Summary of petrographic features for late-Variscan intrusives and dikes from Sàrrabus igneous massif (south-eastern Sardinia, Italy)

Rock-types	Rock-textures	Fundamental phases	Accessory phases	Late-stage
Latest mafic dikes (tholeiitic basalts)	Porphyritic Sub ophitic	Ol + Pl → Cpx + Pl ± Hbl Pl + Cpx ± Ol + Qz	Ti-Mt + Ilm + Sulf + Ap	Tc + Cc
Mafic dikes (basalts to andesites)	Porphyritic to hypidiomorphic	Pl + Hbl + Qz ± Bt ± Opx ± Cpx	Ti-Mt + Ilm + Sulf + Ap ± All	
Felsic dikes	Microgranular to granophyric	Qz + Kfs + Pl + Bt SF: Qz + Kfs + Pl + Hs + Ann SP: Qz + Kfs + Pl + Bt BNB: Qz + Kfs + Pl + Bt	Zrn + Ap + All + Mnz + Ilm + Mt Aln + Mt + Zrn + Ap Aln + Mt + Zrn Ilm + Ap + Zir	Fl Fl + Ann Bt + Ms + Fe-Chl
Peraluminous felsic dikes	Microgranular/porphyritic	Qz + Kfs + Pl + Bt ± Ms ± And	Ilm + Zrn + Ap ± Mnz	Tum
Peraluminous granite (MM)	Hypidiomorphic	Qz + Kfs + Pl + Bt + Gt + Ms ± Chrd	Ilm + Zrn + Ap ± Mnz	
Gabbroic rocks (CR)	Hypidiomorphic Panhypidiomorphic/Hypidiomorphic Pecilophytic	Mg-Hbl + Pl + Bt + Qz ± Opx ± Cpx Pl + Mg-Hbl + Bt + Qz ± Kfs ± Opx Ol + Opx + Cpx + Pl + Qz	Tit + Mt + Ap + Ilm Ilm + Tit + All + Zrn Mt + Ap	Actin + Cumm Cumm Actin + Prgs
Granodiorites (CR)	Hypidiomorphic	Pl + Kfs + Qz + Fe-Hbl + Bt	Ilm + Ap + Aln + Mon ± Tit	Turnm
Gabbrotonalites (BU)	Hypidiomorphic Porphyritic	Qz + Kfs + Pl + Bt ± Fe-Hbl Pl + Qz + Kfs + Bt + Opx + Cpx Pl + Opx + Cpx ± Hbl → Pl + Bt + Kfs + Qz	Ilm + Zrn + Ap Ilm + Ap + Zrn + Sulf	Turnm Actin + Cumm

CR, BU, MM, BNB, SP and SF refer to, Cala Regina Group and Burcèi, Monte Maria, Bruncu Nicola Bove, San Priamo and Monte Sette Fratelli rock-units reported in Fig. 2. Abbreviations list for mineral phases: Pl = plagioclase; Qz = quartz; Kfs = K-feldspar; Bt = biotite; Hbl = hornblende; Opx = orthopyroxene; Cpx = clinopyroxene; Hs = hastingsite; Gt = garnet; Ms = white mica; And = andalusite; Chrd = cordierite; Ol = olivine; Ilm = ilmenite; Ap = apatite; Mon = monazite; Aln = allanite; Zrn = zircon; Sulf = sulphur; Mt = magnetite; Alb = albite; Fl = fluorite; Ann = annite; Actin = actinolite; Cumm = cummingtonite; Prgs = pargasite; Fe-Chl = Fe-chlorite; Tc = talc. Talc observed in mafic dikes formed at the expense of olivine phenocrysts. Ortho- and clinopyroxene observed in Burcèi gabbrotonalites and gabbroic rocks belonging to Stage 1 show commonly a hypersthene and augitic composition, respectively; they are often replaced by actinolite and cummingtonite.